

Final report for the Katalysatorsimulation (Vertrag Nr. 15.0002.PJ/S122-1359) for 2019-2020 concerning modelling of catalyst behavior in entire cycles, cold starts and comparisons with Real Driving Emissions

P. Dimopoulos Eggenschwiler, V. Papetti

November, 2020

## Veröffentlichte Beiträge 2019-2020

V. Papetti, P. Dimopoulos Eggenschwiler, V. Emmanouil, G. Koltsakis

Analysis of TWC operation characteristics in a Euro6 gasoline light duty vehicle

SAE (Society of Automotive Engineers) Paper, 2019-24-0162, 2019

V. Papetti, P. Dimopoulos Eggenschwiler, A. Della Torre, G. Montenegro, A. Onorati, G. Koltsakis

Heat Transfer characterization of Catalytic Converter Substrates during Warm-up

SAE (Society of Automotive Engineers) Paper, 2019-24-0163, 2019

A. Gambarotta, V. Papetti, P. Dimopoulos Eggenschwiler

Analysis of the Effects of Catalytic Converter on Automotive Engines Performance through Real-Time simulation models

Frontiers in Mechanical Engineering, Engine and Automotive Engineering (open access), Front. Mech. Eng., <https://doi.org/10.3389/fmech.2019.00048>

T. Cerri, G. D'Errico, G. Montenegro, A. Onorati, G. Koltsakis, Z. Samaras, V. Tziolas, N. Zingopis, K. Michos J. Rojewski, V. Papetti, P. Dimopoulos Eggenschwiler, P. Soltic

A 1D co-simulation approach for the prediction of pollutant emissions of internal combustion engines

Proceedings of the 19th Stuttgart International Symposium, Automotive and Engine Technology, 2019

V. Papetti, P. Dimopoulos Eggenschwiler

Reduction of Cold Start emissions with Microwave heated Catalytic converters

Proceedings of the 19th Stuttgart International Symposium, Automotive and Engine Technology, 2019

Under Review:

V. Papetti, P. Dimopoulos Eggenschwiler, A. della Torre, G. Montenegro, A. Onorati, A. Ortona, G. Koltsakis

Instationary Heat and Mass Transfer phenomena in Additive Manufactured Open Cell Polyhedral Structures for Automotive Catalysis, Open Cell Polyhedral Structures.

Chemical Engineering Science or its open access mirror

Ref: CES-D-20-01857

# Content

## 1. Executive Summary

## 2. Methodology

### 2.1 Converter Geometries

### 2.2 Detailed Simulation Model

### 2.3 Simulation in the commercial software Axisuite

### 2.4 Analytical Model Equations and Assumptions

### 2.5 Dimensionless quantities and approximation possibilities

### 2.6 Reactions Modeling

## 3. Results

### 3.1 Temporal evolution of temperature inside the HC catalytic converter, detailed simulations

### 3.2 Spatial distribution of temperature inside the HC catalytic converter, detailed simulations

### 3.3 Characteristics of the instationary heat transfer with dimensionless approach, analytical approach based on the detailed simulations

### 3.4 Temporal evolution of species concentration inside the HC catalytic converter, detailed simulations

### 3.5 Reciprocal influence of the different pollutants and the related reaction mechanisms, simulations with Axisuite

### 3.6 Additive Manufactured (AM) catalytic converters, detailed simulations

### 3.7 Evaluation of Possible Cold Start Emission Mitigation Strategies through heating, detailed simulations

### 3.8 Simulations of entire WLTC cycle: comparison between experiments and simulations

#### 3.8.1 THC emission peaks during warm phase

#### 3.8.2 NO emission peaks during warm phase

#### 3.8.3 Cold start emissions

#### 3.8.4 THC cold start emissions

#### 3.8.5 NO cold start emissions

#### 3.8.6 Analysis of the sensitivity of result emissions to $\lambda$ variation

#### 3.8.7 Effects of different PGM loadings of the catalyst

### 3.9 Simulations of other driving cycles

# 1. Executive Summary

In the present project, a combined simulation approach has been followed in order to assess the behavior of automotive catalysts under different aspects. In a first step, detailed simulations have been developed in order to in-depth understand the involved physical and chemical phenomena and to parametrize a dedicated commercial software package. In a further step, the resulting commercial package was used to assess vehicle behavior, simultaneous abatement of all pollutant classes during entire vehicle cycles. Tuning of both simulation paths has been achieved with real vehicle measurements on a chassis dynamometer.

The work involved aimed in examining a series of different effects:

- Emissions during cold starts and their dependencies
- Assessment of cold start emission mitigation strategies
- Assessment of conventional, honeycomb, catalyst substrates in respect to new additive manufactured polyhedral lattice substrates
- Assessment of the influence of several critical aspects in catalyst design: precious metals amount, oxygen storage components, coating amount and composition.

## Cold start phenomena

A series of base case simulations aimed in analyzing the heat and mass transfer processes and chemical reactions during cold starts as well as identifying ways of accelerating the catalyst warm-up and reducing the associated emissions. In order to study the fundamental mechanisms involved, the cases investigated have been setup with exhaust gas of constant, moderate temperatures and mass flow rates entering a catalyst with initial lower temperatures. Detailed simulations in OpenFOAM involved only the oxidation of CO. Simulations of these "standard cases" have been performed with commercial software package (parametrized with the results of the detailed simulations and targeted vehicle experiments) for assessing all pollutant reactions and their mutual interactions.

In all examined cases, including different temperatures, exhaust gas mass flows as well as catalyst substrates (honeycomb and Additive Manufactured polyhedral lattices), two phases during the heat-up have been distinguished:

- In the initial phase, the gases warm-up the solid-converter (convection from fluid to solid aided by initial oxidation reactions). The heat up is assisted by initial oxidation reactions in the upstream converter part.
- The second phase starts when the converter and the fluid inside have reached the same temperature, equal to the one of the fluid entering the converter. This phase is characterized by the heat released by the reactions, thus the heat transferred from the solid to the fluid.

In the first instants of the initial phase, the gases warm-up the solid catalytic converter in the entrance region and are cooled down towards the initial solid temperature in the downstream. Main characteristics of this phase are:

- The duration of the first phase is different along the converter and downstream locations experience a longer first phase. However, the duration is independent from the initial temperature difference between solid and fluid.
- The heat transferred (in energetic terms) is relatively homogeneously distributed throughout the catalytic converter and, in any location, it increases in time towards a peak and decreases thereafter. The heat exchanged is strongly dependent from the initial temperature difference between solid and fluid.
- At each instant, temperatures decrease along the converter length.

- Increasing exhaust gas mass flow accelerates the initial heat up.
- The introduction of dimensionless temperature differences, dimensionless time and dimensionless space coordinates evidences the similarity of all examined cases (i.e. for different mass flow rates, flow inlet and catalytic converter initial temperatures as well as lengths).
- The catalytic converter heat up, expressed with the dimensionless parameters, has the characteristic S-type shape, and is a double logarithmic function that can be approximated by a corresponding analytical expression. A larger converter heats up slower at first but later at an accelerated rate.

The second phase is characterized by:

- The driving phenomena are chemical reactions. As upstream locations are warmed-up first, the onset of chemical reactions first occurs upstream. The heat released by the reactions is transported downstream resulting in a faster increase of temperatures and reaction rates (as long as enough reactants are there). Stationary conditions are reached almost instantly, leading to constant local temperatures and reaction rates in time.
- Temperatures are generally higher in the downstream than in the upstream converter part. This leads to higher reaction rates and thus to higher reaction heats released in the downstream locations.
- The temperature in locations where identical conversion is achieved is a function only of the inflowing CO concentration and is independent of the fluid mass flow.
- Increasing fluid mass flow results in lower local temperature increase in respect to the temperature of the inflowing gases.
- The enthalpy of the inflowing gases has to be matched to the energy released by the chemical reactions, for achieving highest temperatures in upstream locations. If the mass flow is too high, only a modest and slow temperature increase can be achieved.

Additive Manufactured substrates provide, in addition to honeycombs, optimization possibilities by changing the basic geometrical parameters. A series of dedicated simulations aimed at highlighting their influence on the cold start characteristics:

- Lighter structures (higher  $\epsilon$ ) allow a faster initiation of the warm up, have shorter first phase duration and require less heat exchanged for reaching a target temperature.
- Structures characterized by higher Nu levels show a faster warm up, have shorter first phase duration and require less heat exchanged for reaching a target temperature.
- During the second phase of the warm up process, after reaching stationarity, when the main phenomena are the chemical reactions and the consequent heat released from the solid surface to the fluid, the AM behavior is almost independent from Nu, mass and surface properties.

With the developed analytical approach for the initial catalyst heat-up phase, it is possible to compute not only the heat-up, but also the emissions during this phase in a very easy manner. However, as soon as reactions release significant amounts of heat, the temperature increases and this in turn increases reaction rates in an exponential manner. Here any further solution without solving the differential equations is only a very crude approximation.

Simulations involving all pollutant classes have a significant higher cost (in CPU time). Therefore, the commercial software package Axisiute has been used. A reaction mechanism involving 19 reactions has been developed and parametrized in order to match the emission characteristics of a measured catalyst on a vehicle chassis dynamometer. The simulations have shown: first reactions occurring during cold

start are NO<sub>x</sub> reduction (with CO and Ce<sub>2</sub>O<sub>3</sub>) and hydrocarbon steam reforming. The latter produces CO and H<sub>2</sub>, which is then oxidized to H<sub>2</sub>O with significant heat release, while the former does not affect the heat balance. These interactions among the different chemical reactions have to be taken into account for obtaining reliable simulation results, although they lead to a complex system of ordinary differential equations.

For the CO abatement:

- The main mechanism is direct oxidation.
- Reaction with NO is somehow half an order of magnitude weaker.
- Ceria catalyzed oxidation is somehow an order of magnitude weaker.
- Almost of the same order of magnitude CO is produced, by ceria catalyzed C<sub>3</sub>H<sub>6</sub> partial oxidation.

C<sub>3</sub>H<sub>6</sub> abatement can only evolve after catalytic sites are freed from CO and is more pronounced in lean and less in rich mixtures as a result of:

- Direct oxidation
- Ceria catalyzed C<sub>3</sub>H<sub>6</sub> partial oxidation (an order of magnitude weaker in respect to direct oxidation)
- C<sub>3</sub>H<sub>6</sub> steam reforming, being even two orders of magnitude weaker, but playing an essential role in the catalyst heat-up as it produces H<sub>2</sub>, which oxidizes to water under substantial heat release aiding the heat-up.

NO<sub>x</sub> reduction at the low temperatures is mainly due to:

- the reduction through CO
- the catalytic reduction on ceria sites (about one order of magnitude weaker)

Further detailed simulations have assessed the effectiveness of different cold start emission mitigation strategies based on either heating the fluid before entering the converter (for instance with an electric heater), or directly heating the converter (for instance with microwaves). The investigations showed that efficient heating is achieved when the light-off temperature of the pollutants is reached in the upstream catalyst part, initiating enough chemical reactions, which, in turn, release enough heat, that is not entirely convected to the flowing gases. At the lower exhaust mass flows, heating the exhaust gases leads to lower cold start emissions in respect to preheating the solid material of the catalyst. With increasing exhaust mass flows, cold start emissions decrease when heating the catalyst, while increase when heating is applied to the exhaust gases.

#### Derivation of a general, simplified chemical reaction mechanism based on vehicle chassis dynamometer measurements and simulations

Simulations of entire vehicle cycles had the aim to analyze the processes in the catalyst during high emission periods. Based on vehicle measurements, a set of 19 chemical reactions has been identified and parametrized in order to reproduce the vehicle emission over the cycle. Further simplification (lower number of reactions) increased the deviation of the simulations from the measurements significantly. It is expected, that additional chemical reactions (considerations of additional unburnt hydrocarbons, apart from C<sub>3</sub>H<sub>6</sub>) will improve the accuracy of the simulations.

Cycle emissions comprise mainly the cold start contribution as well as discrete emission break-through events during transients. At high temperatures:

- CO and THC break-throughs lead to discrete and simultaneous peaks.

- Each discrete peak of CO and THC follows a fuel cutoff phase. During the reacceleration, a rich combustion phase in the engine occurs and O<sub>2</sub> is consumed, thus inhibiting direct oxidation. Only ceria reactions assist oxidation as long as CeO<sub>2</sub> sites are not fully depleted.
- NO peaks are associated to phases with high oxygen amounts in the catalyst: the main mechanisms are reduction with CO, surface ceria reactions and with H<sub>2</sub>. At high NO concentrations coming from the engine, reaction rates are not strong enough for completing reduction.

During cold starts, it is noticed that:

- CO, THC and NO peaks are simultaneous. CO and THC peaks are due to lack of O<sub>2</sub> and surface ceria, similarly to the phenomena characteristic in the warm phase. NO peaks are due to lack of CO available and surface ceria.

The effects of varying O<sub>2</sub> content are investigated: higher  $\lambda$  value increases NO emissions. In fact, there is less CO available for NO reductions.

When varying precious metal content: lower PGM loading increases CO and THC cumulative emissions, while the impact on NO emissions is negligible. Moreover, higher PGM leads to a reduction in direct oxidation rates, while an increase in ceria reactions rates.

With the derived reaction mechanism, a series of further vehicle cycles have been simulated. While the emission events have been well predicted, the emitted values have mainly been underpredicted.

## 2. Methodology

Two different approaches have been chosen in order to understand and analyze catalyst behavior:

1. Detailed own simulations based on the free software OpenFOAM
2. Simulations using the commercial software Axisuite with parameters tuned by targeted measurements of real catalysts on the chassis dynamometer

With the former, processes were simulated in a detailed level providing knowledge of the heat and mass transfer as well as on uncoupled chemical reaction mechanisms, i.e. abatement of single pollutants. These simulations have been also used for verification of the commercial code [1]. However, the computational cost for the detailed simulations is very high, therefore only limited engine operating conditions have been in focus, while entire vehicle cycles would result in excessive run times. For these cases we used the latter, i.e. the commercial Axisuite. On Axisuite, entire vehicle cycles can be simulated within a couple of minutes including all the relevant pollutants their reactions mechanisms as well as their mutual interactions.

For the initial phase of the catalyst heat-up, as long as the gases heat up the solid and the contribution of chemical reactions in terms of heat is negligible, an analytical approach could be developed and compared to measurement and detailed simulations.

### 2.1 Converter Geometries

Different catalytic geometries and dimensions have been considered, both of benchmark honeycomb (HC) and of innovative Additive Manufactured (AM) open cell polyhedral configurations. For the HC benchmark, a TWC 600 cpsi, 2.5mil honeycomb is modeled (main geometrical properties are described in Table 1). Concerning AM substrates, three different geometries are compared. The assumed unitary cell is cubic rotated 45° so that one spatial diagonal of the cube is aligned to the main gas flow. This geometry was identified to be optimal. This elementary cell is called C45, while the three different AM analyzed are denoted by AM1, AM2 and AM3. Their main geometrical properties are described in Table 2. Geometrical properties have been computed based on the model in [2][3]. The converter material is cordierite.

Table 1: Geometrical properties of the HC structures simulated.

	$\epsilon$ [-]	$d_s$ [mm]	$L_c$ [mm]	$S_v$ [m <sup>2</sup> /m <sup>3</sup> ]
600 cpsi, 2.5mil	0.84	0.125	1.25	3540

Table 2: Geometrical properties of the AM structures simulated.

	Unitary cell	$\epsilon$ [-]	$d_s$ [mm]	$L_c$ [mm]	$S_v$ [m <sup>2</sup> /m <sup>3</sup> ]
AM1	C45	0.8	0.8	2.08	896
AM2	C45	0.9	0.5	3.43	733
AM3	C45	0.85	0.5	2	1050

### 2.2 Detailed Simulation Model

A catalyst substrate is simulated in OpenFOAM with a multi-region approach, distinguishing the fluid and the coated substrate (catalytic converter region), thus the fundamental equations for the fluid and the catalytic converter regions are solved on different meshes. The two grids are overlapping where both

gas phase and solid phase coexist, for example in the catalyst porous regions, while in the pipe/cone regions only the fluid mesh is defined. The volume occupied by each phase is defined by a volumetric fraction coefficient computed as the ratio between the volume occupied by the corresponding phase and the total volume. The coupling between the two regions is managed between own sub-models, which describe the mass and heat transfer between fluid and catalyst regions. On the solid region, the species and energy conservation equations are solved; on the fluid region, the set of governing equations of conservation of mass, momentum, energy and species is closed with the perfect gas equation of state. The thermal properties of the multi-component mixture are determined on the basis of the JANAF tables. A Sutherland model is applied for the computation of the transport properties, in order to take into account the temperature dependence of viscosity. The mass diffusivity is modeled under the assumption of Schmidt number equal to 1 in order to reduce the computational burden. The chemistry is modelled with Langmuir-Hinshelwood-type expression in which the reaction rate parameters have been previously tuned with experiments. The permeability model that defines the fluid-dynamic resistance encountered by the fluid flowing through the porous medium depends on the geometrical properties of the substrate and the instantaneous fluid dynamics conditions. It is determined on the basis of Reynolds number ( $Re$ ) with correlations in the form  $\Pi_p = F(Re, d_f)$  by results of own numerical simulations at the micro scales [3][4][5]. Specific correlations of  $Nu$  and  $Sh$  in function of  $Re$  are exploited to specify the transfer of heat/mass on the basis of the actual fluid-dynamic conditions and the properties of the fluid/solid. Even in this case, the correlations in the form of  $Nu = F(Re, Pr, d_f)$  and  $Sh = F(Re, Sc, d_f)$  are results of previous simulations performed by the present authors [3][4][5]. The catalyst is treated as a generic porous medium characterized by some general parameters: porosity  $\epsilon$ , the specific surface  $S_v$ , the characteristic size of the pores/channels open to the fluid  $d_f$  (in the three directions, if the media is anisotropic), the characteristic size of the solid structure/walls of the substrate  $d_s$ , the washcoat thickness  $d_w$ . These parameters are then exploited in the other submodels to calculate the actual fluid dynamics and heat/mass transfer properties on the basis of suitable correlations for the specific medium.

For cold start assessment and comparisons, a set of standard cases has been defined. The typical automotive catalyst cold start is characterized by gases arriving in the entrance of the catalytic converter (coming from the engine) at moderate temperatures. In order to analyze and compare the fundamental mechanisms involved, the cases in this study have been setup based on the following pattern: exhaust gas of constant temperature  $T_{Fin}(x=0)$ , and mass flow rates  $\dot{m}_F$  flowing in a catalytic converter with an initial, lower and uniform temperature  $T_S(t=0) = T_{S0}$ . The temporal and spatial evolution of temperatures and concentrations, as well as of further characteristic properties of the heat and mass transfer are the main focus.

### 2.3 Simulation in the commercial software Axisuite

The dimensions of the catalytic converter have been specified in terms of length and frontal circular area (diameter) and have been discretized with a 1D mesh. In this 1D mesh discretization, all the channels are assumed to behave identically. The overall catalytic converter volume is about 2l. The substrate material is cordierite, a washcoat loading of 250g/l has been considered. Initial zero concentration for ceria, is modelled.

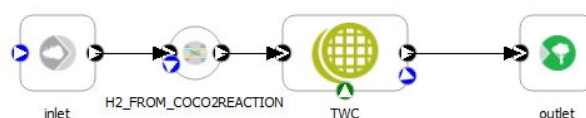


Fig. 1. Axisuite system layout.

The reaction scheme library has been developed starting from a built-in common library present in the environment of Axisuite. In order to tune the simulations so that they agreed with measurements on the chassis dynamometer, 19 individual reactions had to be taken into account. The pre exponential factor

and the activation energy of each reaction have been tuned with experimental data from chassis dynamometer measurements on a vehicle in order to fit the experimental results. The proper parameters have been decided by analyzing the reaction rates of all the reactions as a function of time. The considered reactions are grouped in 5 types (Table 3):

- P(latin) G(roup) M(etals) O<sub>2</sub> (oxidation of CO, HC, NO on PGM sites),
- PGM NO<sub>x</sub> (reduction of NO<sub>x</sub> by CO, HC, H<sub>2</sub> on PGM sites),
- PGM H<sub>2</sub>O (steam reforming and water-gas shift reaction),
- surface Ceria reactions (reactions for O<sub>2</sub> storage on Ce sites occurring fast, on the surface),
- and bulk Ceria reactions (reactions for O<sub>2</sub> storage that occur slower after diffusion in the wash-coat layer).

The PGM reactions are modelled as reversible substrate reactions with a Langmuir-Hinshelwood rate expression. In the Langmuir-Hinshelwood rate expressions, inhibition terms, G, are used in the denominator, to account for the competition of the various species to occupy the active catalytic sites. The inhibition terms of oxidation reactions are based on the pioneering work of Voltz et al. on Pt catalysts [6].

Table 3. List of the minimal set of chemical reactions necessary in order to reproduce the catalyst activity as measured on a vehicle on the chassis dynamometer.

Group	Reaction Group	Reactions	NR
I	PGM O <sub>2</sub>	$\text{CO} + 1/2 \text{O}_2 \rightarrow \text{CO}_2$	1
		$\text{H}_2 + 1/2 \text{O}_2 \rightarrow \text{H}_2\text{O}$	2
		$\text{C}_3\text{H}_6 + 9/2 \text{O}_2 \rightarrow 3 \text{CO}_2 + 3 \text{H}_2\text{O}$	3
II	PGM NO <sub>x</sub>	$\text{C}_3\text{H}_6 + 9 \text{NO} \rightarrow 3 \text{CO}_2 + 3 \text{H}_2\text{O} + 9/2 \text{N}_2$	4
		$\text{CO} + \text{NO} \rightarrow \text{CO}_2 + 1/2 \text{N}_2$	5
		$\text{H}_2 + \text{NO} \rightarrow \text{H}_2\text{O} + 1/2 \text{N}_2$	6
III	PGM H <sub>2</sub> O	$\text{C}_3\text{H}_6 + 3 \text{H}_2\text{O} \rightarrow 3 \text{CO} + 6 \text{H}_2$	7
		$\text{CO} + \text{H}_2\text{O} \rightarrow \text{CO}_2 + \text{H}_2$	8
		$\text{CO}_2 + \text{H}_2 \rightarrow \text{CO} + \text{H}_2\text{O}$	9
IV	Ceria reactions	$b\text{Ce}_2\text{O}_3 + 1/2 \text{O}_2 \rightarrow 2 b\text{CeO}_2$	10
		$b\text{Ce}_2\text{O}_3 + \text{NO} \rightarrow 2 b\text{CeO}_2 + 1/2 \text{N}_2$	11
		$2 b\text{CeO}_2 + \text{CO} \rightarrow b\text{Ce}_2\text{O}_3 + \text{CO}_2$	12
		$2 b\text{CeO}_2 + \text{H}_2 \rightarrow b\text{Ce}_2\text{O}_3 + \text{H}_2\text{O}$	13
		$2 b\text{CeO}_2 + 1/6 \text{C}_3\text{H}_6 \rightarrow b\text{Ce}_2\text{O}_3 + 1/2 \text{CO} + 1/2 \text{H}_2\text{O}$	14
V	Fast Ceria reactions	$s\text{Ce}_2\text{O}_3 + 1/2 \text{O}_2 \rightarrow 2 s\text{CeO}_2$	15
		$s\text{Ce}_2\text{O}_3 + \text{NO} \rightarrow 2 s\text{CeO}_2 + 1/2 \text{N}_2$	16
		$2 s\text{CeO}_2 + \text{CO} \rightarrow s\text{Ce}_2\text{O}_3 + \text{CO}_2$	17
		$2 s\text{CeO}_2 + \text{H}_2 \rightarrow s\text{Ce}_2\text{O}_3 + \text{H}_2\text{O}$	18
		$2 s\text{CeO}_2 + 1/6 \text{C}_3\text{H}_6 \rightarrow s\text{Ce}_2\text{O}_3 + 1/2 \text{CO} + 1/2 \text{H}_2\text{O}$	19

## 2.4 Analytical Model Equations and Assumptions

The analytical model is of a single channel inside the monolithic configuration (Fig. 2) and takes into account the gas-solid convective heat and mass transfer, longitudinal thermal conductivity and heat capacity effects in the solid phase. The model neglects the radial variations of the gas-phase temperature, concentration, and velocity within the channel so that these variables are to be interpreted as cross-sectional averages. Accumulation of mass and heat in the gas phase is neglected (fluid time constants are typically much smaller than that of the solid thermal response [7]). This implies quasi-steady state condition for the fluid phase, considering temporal changes only characteristics for the solid. The wall heat capacity is large compared with the heat capacity of the fluid. Thus, during a small time increment, only the effect of varying wall temperature needs to be taken into account and the fluid heat capacity effect can be ignored [7]. Heat transfer to the ambient in the warm up phase was considered as negligible, since during warm up, temperature differences between the catalytic converter and the ambient are

small. The channel is considered to be initially at a constant temperature,  $T_S(t=0)=T_{S0}$ , the feed gas enters the duct at a constant inlet temperature  $T_{Fin}$  ( $T_{Fin} > T_S$ ) and constant mass flow  $\dot{m}_F$ . The analysis will focus on the temporal evolution of the solid and fluid temperature at different positions along the catalytic converter.  $T_F$  and  $T_S$  are function of time and space.

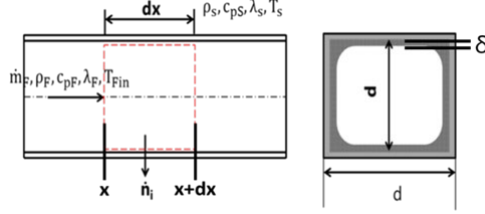


Fig. 2. Schematic of the analytical model.

## 2.5 Dimensionless quantities and approximation possibilities

The effects on temperature profiles for solid and gas and the species concentrations in space have been analyzed with a non dimensional approach. The approach followed is based on concepts introduced in heat transfer [8], as well as in [9]. The struts/channel walls are considered as very thin (usually less than 0.5mm), so that no radial solid-phase temperature gradients are expected. For the heat transfer cases met in catalytic reactors, the wall heat capacity is large compared with the heat capacity of the fluid. Thus, during a small-time increment, only the effect of varying wall temperature needs to be taken into account and the fluid heat capacity effect can be ignored [8]. The assumption of quasi-steady state heat transfer has been widely used in literature ([9][10][11]). Radiation effects are not included, since they are not significant in the case of low temperatures [12]. Moreover, in accordance with [13], in the mass flow range considered, axial gas conduction effects are excluded. Assuming quasi-steady state, incompressible flow, considering an infinitesimal volume of the fluid phase, in the case when chemical reactions have not a significant contribution, the solid energy balance during the transient can be formulated as:

$$\frac{\partial T_S}{\partial t} = \frac{\lambda_S}{\rho_S c_S} \frac{\partial^2 T_S}{\partial x^2} + \frac{\dot{m}_F c_{pF}}{A_{S,FRONT} \rho_S c_S} \frac{\partial T_F}{\partial x} \quad (1)$$

While the corresponding fluid energy balance as:

$$\frac{\partial T_F}{\partial x} = - \frac{4Nu\lambda_F}{\dot{m}_F c_{pF}} (T_F - T_S) \quad (2)$$

Dimensionless fluid and solid temperature differences can be introduced according to ( $T_F$  and  $T_S$  are function of time and space, thus even  $\theta_S$  and  $\theta_F$  are function of time and space):

$$\theta_S = \frac{T_S - T_0}{T_{F,in} - T_0} \quad (3)$$

$$\theta_F = \frac{T_F - T_0}{T_{F,in} - T_0} \quad (4)$$

Please notice that  $T_F$  and  $T_S$  are function of time and space, thus also  $\theta_F$  and  $\theta_S$ . The reference temperature was chosen for simplicity as the initial solid temperature. Dimensionless fluid temperature  $\theta_F$  represents the ratio between the instantaneous solid-fluid temperature difference to the initial solid-fluid temperature difference. Under the hypothesis of negligible reactions, which is true in the first period of the warm-up, dimensionless solid temperature represents the increment of solid temperature difference with respect to the maximum increment it can reach. Moreover, a dimensionless length,  $\xi$ , similarly to [8], as well as a dimensionless time,  $\tau$ , can be introduced:

$$\xi = \frac{4Nu\lambda_F x}{\dot{m}_F c_{PF}} = NTU_\theta \quad (5)$$

$$\tau = \frac{4Nu\lambda_F t}{A_{S,FRONT} \rho_S c_S} \quad (6)$$

Clearly,  $\xi$ , corresponds to the number of transfer units  $NTU_\theta$ .

Where:

$c_{PF}$  Specific fluid heat capacity [J/(kg·K)]

$c_S$  Specific solid heat capacity [J/(kg·K)]

$\lambda$  Thermal conductivity [W/(m·K)]

$\dot{m}_F$  Mass fluid flowrate [kg/s]

$Nu$  Nusselt number

$\rho_S$  Solid density [kg/m<sup>3</sup>]

$t$  Time [s]

$x$  Space coordinate in main flow direction [m]

Similarly a dimensionless conductivity  $\Lambda$  can be introduced:

$$\Lambda = \frac{4Nu\lambda_F A_{S,FRONT} \lambda_S}{\dot{m}_F^2 c_{PF}^2} \quad (7)$$

Using Eqs. 3-6 simplifies Eqs. 1-2, to:

$$\frac{\partial \theta_F}{\partial \tau} = \theta_S - \theta_F \quad (8)$$

$$\frac{\partial \theta_S}{\partial \tau} = \Lambda \frac{\partial^2 \theta_S}{\partial \xi^2} - \frac{\partial \theta_F}{\partial \xi} \quad (9)$$

## 2.6 Reactions Modeling

The emissions concentrations are result of chemical reactions, species mass conservation and species diffusion through the washcoat model. The chemistry is modelled according to Langmuir-Hinshelwood theory:

$$r = \frac{A \cdot e^{-\frac{E_j}{RT}} \cdot \prod_i^{1..n_r} X_i}{G_R} \quad (10)$$

Where A is the pre exponential factor, i-th the species (reactants and products), E the activation energy, while G is the inhibition factor that takes into account the impact on the overall kinetics of the adsorption and desorption competition among reactants and products on the active sites. This term is directly proportional to the washcoat temperature.

The species conservation equation is:

$$\frac{\partial X_{i,F}}{\partial t} + u_\infty \frac{\partial X_{i,F}}{\partial x} = r_{iS} \quad (11)$$

Where  $X_{i,F}$  represents the species concentration in the fluid (F), while  $r_{i,S}$  is the reaction rate of the species  $i$ -th on the converter surface (S). Species concentration in the solid phase is different from species concentration in the fluid due to the number of moles that diffuse to the washcoat pores. The number of moles that diffuse to the washcoat pores is a function of the species concentration gradient. Thus the equation would be implicit and an iterative algorithm would be required. In order to simplify this calculation, it has been assumed that there is no accumulation of mass inside the washcoat and that the chemical compounds that diffuse into the pores, react on the active sites of the converter.

From Eqs. 10-11, it is thus possible to derive the following equation:

$$r_i = k_{m,i}(X_{i,F} - X_{i,S}) \quad (12)$$

Where  $k_{m,i}$  is the mass transfer coefficient of the  $i$ -th species, which is a function of the Reynolds and of the Schmidt number, of the hydraulic diameter, of the active catalytic surface, and of the species diffusion coefficients, which is also depending on the species concentrations.  $K_m$  can also be defined as:

$$k_{m,i} = \frac{Sh D_i}{d_F} \quad (13)$$

The iterative procedure to calculate the solid concentration of the reactants may be computationally demanding if the simulation of a long real time period is addressed. To achieve a reduction of the computational time, a simplified approach was developed on the basis of the Baruah's theory. The main assumption is that when the global kinetics becomes controlled by the mass transfer process, all reactants diffusing into the washcoat are going to react on the active sites and consequently their concentration in the solid phase can be considered small. This means that the concentration gradient between the gas phase and the solid phase of the reactants can be approximated to the gas phase concentration itself.

The final equation becomes:

$$\frac{dX_{i,F}}{dx} = \frac{Sh D_i}{d_F u_\infty} (X_{i,F} - X_{i,S}) \quad (14)$$

Thus, the total mass flux of the specie in question (where  $i$ -th species is CO) transferred from the fluid to the solid, being equal to the mass reacting on the wall, can be obtained by:

$$\dot{m}_{rCO,j} = \frac{\dot{m}_F M_{CO}}{M M_F \Delta V} (X_{CO,F,j} - X_{CO,F,j+1}) \quad (15)$$

Where  $j$ -th indicates a generic position according to the spatial discretization. This assumption is realistic for steady-state operation, but not necessarily for operation under highly transient temperature and composition conditions.

Especially during cold starts, it is really important to compute the species concentrations both on the converter wall and in the fluid. The detailed computation is performed for one species, CO, in OpenFOAM environment, where the mass, energy and species conservation equations are numerically solved. More than one reaction is instead modelled in the commercial software Axisuite with some simplifications. The assumption is infinite fast reaction, thus the mass transfer limitations at the wall are neglected (whatever arrives to the wall, it reacts). The quasi-steady approach expressed by Eq. 14 is retained, aiming at keeping model complexity, and thus flexibility, to acceptable levels.

### 3. Results

#### 3.1 Temporal evolution of temperature inside the HC catalytic converter, detailed simulations

For the sake of simplicity, we have extracted the results of fluid and solid phase at five different positions along the mesh length: these correspond to inlet ( $x=0$ ), one quarter of the length ( $x=1/4L=0.038m$ ), half of the length ( $x=1/2L=0.076m$ ), three quarters of the length ( $x=3/4L=0.1148m$ ) and exit length ( $x=L=0.1524m$ ). Fig. 3a represents the case of fluid entering with  $T_{Fin}=410K$ ,  $\dot{m}_F=0.0043kg/s$ ,  $T_S(t=0)=T_{S0}=260K$ . Solid lines represent the temperature of the fluid while dashed lines the temperature of the solid (in all the Figures).

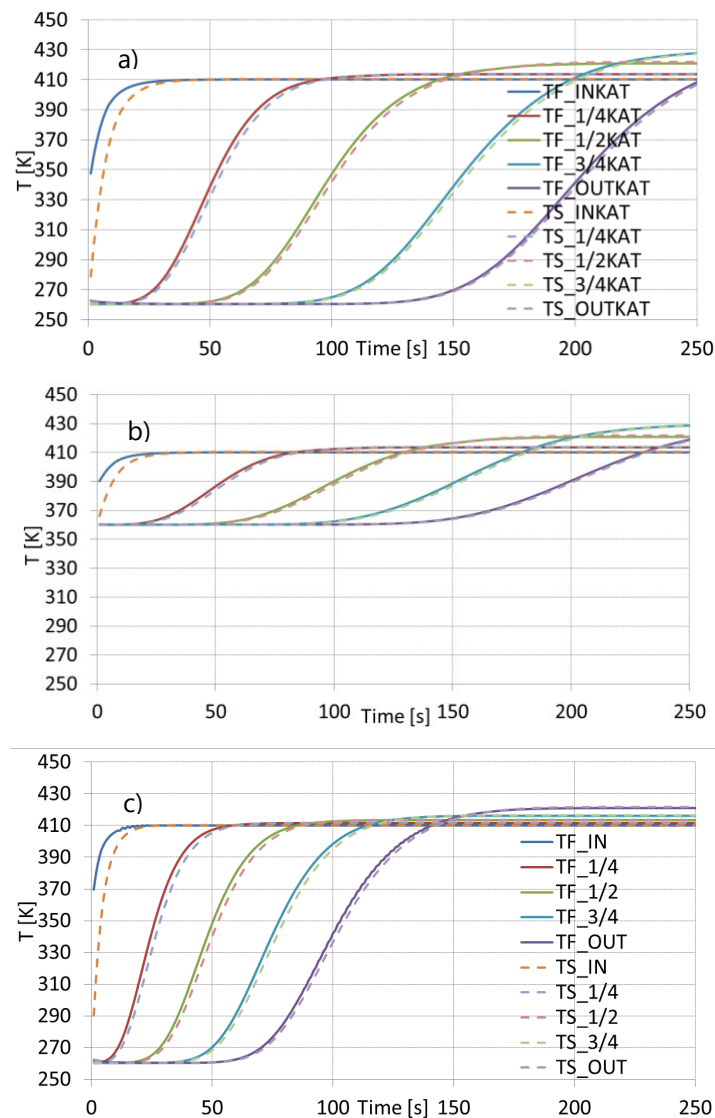


Fig. 3. Fluid (solid lines) and catalyst (dashed lines) temperature time histories in different locations inside the catalytic converter,  $T_{Fin}=410K$  and  $\dot{m}_F=0.0043kg/s$  in (a,b),  $\dot{m}_F=0.0086kg/s$  in (c),  $T_{S0}=260K$  in (a,c) and  $360K$  in (b).

In the entrance of the catalytic converter, the fluid is instantly cooled down, to a temperature of  $350K$  in a) and  $390K$  in b) resulting based on the thermal effusivities involved. Thereafter (still taking the entrance only into account) fluid and solid heat up, until the temperature of the fluid reassumes its inflowing

temperature and the temperature of the solid reaches the temperature of the fluid. As the gas flows through the downstream catalyst parts, it is further cooled down towards the solid initial temperatures. So, for  $t < 30s$ ,  $T_F(x=1/4L) = T_{S0}$  and in a similar manner for  $t < 50s$   $T_F(x=1/2L) = T_{S0}$  as well as for  $t < 100s$   $T_F(x=3/4L) = T_S(t=0)$ .

Based on these observations and also all of the cases examined, the catalyst warm-up can be divided in two different phases. The initial phase with heat transferred from the fluid to the solid (convection)  $T_S < T_F < T_{Fin}$ , until  $T_S = T_F = T_{Fin}$ . In this phase, temperature in downstream locations are lower than in the upstream (at the same  $t$ ). Following this, the second phase starts as soon as  $T_F > T_S$ . Here the heat-up is primarily based on the heat released by the chemical reactions in the solid. The heat released by the reactions results in solid temperatures higher than the fluid temperatures, thus the heat transfer is from the solid to the fluid and  $T_S > T_F > T_{Fin}$ . Certainly, first, weak chemical reactions have initiated earlier. Indeed, first oxidation reactions occur in the very first part of the catalytic converter as soon as  $T_S \geq 373K$ . The heat produced by the chemical reactions is transferred to the fluid (convection) as well as conducted inside the solid (as long as solid downstream parts have lower temperatures). A local equilibrium is reached almost instantly, exhibiting stationary temperatures at each location. The heat generated is taken up by the fluid and contributes to the heat up of the downstream catalyst sections, which, in turn, leads to locally higher reaction rates. Thus, the local temperatures increase in the downstream, in contrast to the first phase. The very small increase of the temperature in the last quarter is due to the low amount of remaining CO, as almost the entire CO is oxidized in the upstream catalyst parts.

Related to the typical heat up process, it can be added that:

- The duration of the initial phase increases at downstream locations.
- The duration of the initial phase is independent from the initial temperature difference between solid and fluid, while the heat exchanged is strongly dependent thereupon.
- The onset of the second phase is mainly affected by the initial solid temperatures and is only weakly affected by the inlet fluid temperature.
- The local equilibrium temperatures and reaction rates are a function of the inlet fluid temperature and of the inlet CO concentration, but not of the initial solid temperature.
- The highest temperature in the converter is reached at the location where the last remaining CO is oxidized. This temperature is a function only of the inflowing CO concentration and is independent of the fluid mass flow.
- The enthalpy of the inflowing gases has to be matched to the energy released by the chemical reactions, for achieving the fastest possible warm up. If the mass flow is too high, only a modest and slow temperature increase can be achieved.

The effects of varying  $T_{S0}$  and  $\dot{m}_F$  have been investigated respectively in Fig. 3b-c. It is evident that the nature of the heat transfer mechanism remains the same. As can be seen by comparing Fig. 3a and b, higher  $T_{S0}$  only slightly accelerates the warm up process. In case b, the catalytic converter is warmer at the beginning, but the driving temperature differences to the gas is lower.

In Fig. 3c, with double  $\dot{m}_F$ . Due to the higher fluid velocity, the heat transfer is stronger and there is a faster solid heat up.

### 3.2 Spatial distribution of temperature inside the HC catalytic converter, detailed simulations

For reactions to start, sufficient high temperatures are required in specific localized points inside the catalytic converter and not in the entire solid phase. In Fig. 4 the data of Figs. 3a-b are plotted over the space coordinate in eight different time instants. In addition, the case with  $T_{S0} = 300K$  has been considered. It is clear that the fluid is cooled down along the flow through the catalytic converter, while warm-

ing the solid (catalytic converter) up; the effects are already evident from the beginning in the first catalyst half, and much more pronounced but later in the second half. At  $t=50s$  the first half of the catalytic converter is been gradually warmed up, while the second half has still the initial temperature.

Temperatures higher than  $T_{Fin}$  are due to exothermic chemical reactions: first reactions are evident very soon in the entrance region, while much later in the downstream catalyst parts. Fig. 4 shows thus where the heat up process is in the first and in the second phase at the different instants considered. Already at  $t=50s$  the first converter section is in the first phase, while downstream the converter is still in the first phase. Only at  $t=200s$  the second half reaches  $T_F > T_{Fin}$ , thus the second phase. In the same way, the last quarter experiences the second phase only after  $t=250s$ .

The impact of different  $T_{S0}$  is evident in the first 150s, and it decreases with time: in the first time span, the temperature gradients along the catalytic converter are higher in the case of the lower  $T_{S0}$ , but the final temperature profiles are almost independent from  $T_{S0}$ . In the same way, higher  $T_{S0}$  only slightly accelerates the change from the first to the second phase.

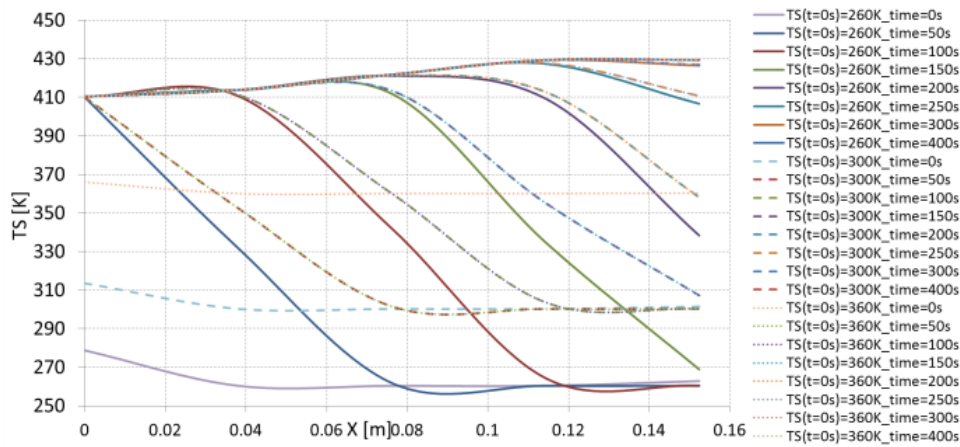


Fig. 4. Solid temperature profile along the catalytic converter length at different time instants,  $T_{Fin} = 410K$  and  $T_S(t=0) = (260, 300, 360)K$ .

### 3.3 Characteristics of the instationary heat transfer with dimensionless approach, analytical approach based on the detailed simulations

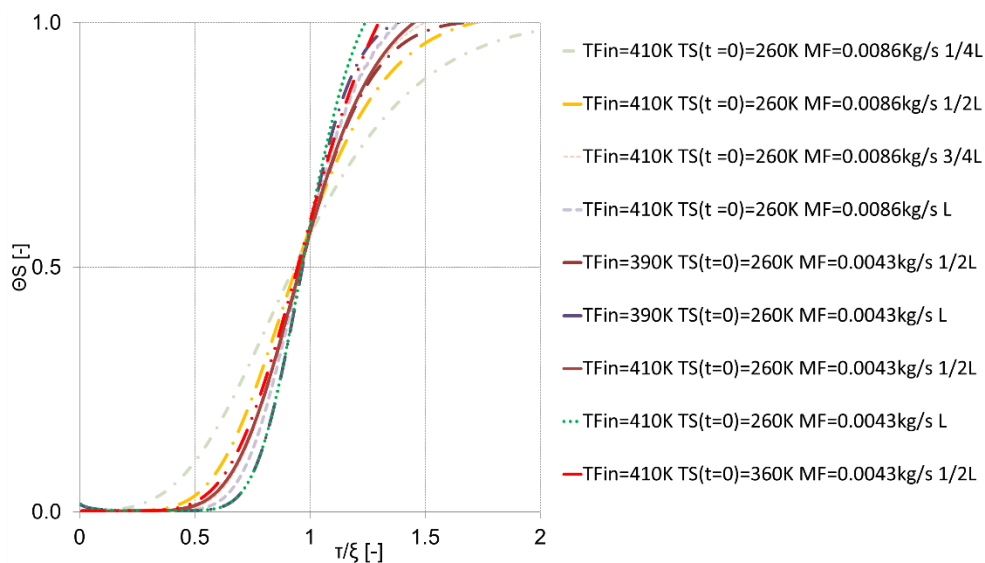


Fig. 5.  $\theta_S$  in function of  $\tau/\xi$ , with  $T_S(t=0) = 260K$ ,  $T_{Fin} = (390, 410)K$ ,  $\dot{m}_F = 0.0043kg/s$  and with  $T_{Fin} = 410K$ ,  $\dot{m}_F = (0.0043, 0.0086)kg/s$ .

Fig. 5 describes the dimensionless temperature response of HC converter,  $\theta_F$ , as a function of the dimensionless time-space coordinate  $\tau/\xi$ . Different lines correspond to different conditions, i.e.  $T_{S0}=[260,360]$ K,  $T_{Fin}=[390, 410]$ K and  $\dot{m}_F=[0.0043, 0.0086]$ kg/s, and to different catalytic converter lengths ( $1/2L$  and  $L$ ). All lines have the characteristic S-shape. The initial  $\theta(T_S=T_S(t=0)=T_0)=0$  and approaches unity ( $T_S=T_{Fin}$ ) at the end of the initial heat-up phase. Values higher than 1 correspond to the second phase of the warm up and are results of heat released by the reactions. Interestingly, the temperature rise for longer catalytic converters occurs later, but it is steeper so that the asymptotic temperature is achieved earlier. Even  $\dot{m}_F$  influences  $\theta_F$  response. The temperature rise for lower  $\dot{m}_F$  occurs later, but it is steeper so that the asymptotic temperature is achieved earlier. Important to notice is that  $\theta_F \approx 0.56$  for  $\tau/\xi$  close to 1. The values we found are very similar to those in [8]. The heat up of a converter can be approximated by an analytical expression using a double exponential function of the type:

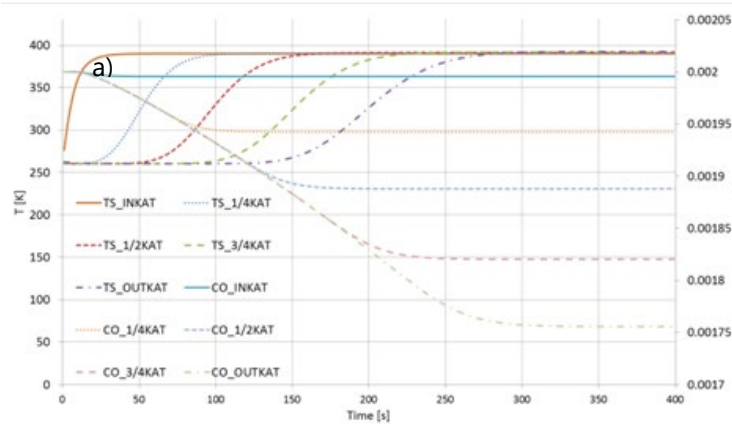
$$\theta = \theta\left(\frac{\tau}{\xi}\right) = 1 - e^{-k\left(\frac{\tau}{\xi}\right)^m} \quad (16)$$

The  $k$  parameter is independent from  $\xi$  and can be found by substituting the point  $(\tau / \xi, \theta)=(1, 0.56)$  in Eq. 16,  $k=\ln(1-0.56)=-0.82$ . Given the differences in the steepness of the lines in Fig. 5, the exponent  $m$  should be a function of  $\xi$ . The method of least-squares approximation has been employed to find the best correlation between  $m$  and  $\xi$ , the result is:

$$m = 1.7 \xi^{-0.18} \quad (17)$$

The implications of Eq. 16 are of some interest for simplifying the numerical approach. First of all, it is clear that an equation similar to Eq. 16 can only describe the phenomena with some accuracy when the second term of Eq. 1,  $\Lambda \frac{\partial^2 \theta_S}{\partial \xi^2}$ , is small relatively to the third one,  $\frac{\partial \theta_F}{\partial \xi}$  (and at negligible heat release due to chemical reactions). This is the case when  $\Lambda$  is small, thus small or negligible axial heat conduction in the solid. This is also the case for the catalytic converter in question (ceramic material) in the present work (it is not the case when considering metallic catalyst substrates). In addition, Eq. 16 gives an analytical solution of the time and location dependent temperatures, should  $m$  and  $k$  be known. So, by knowing  $m$  and  $k$  (through either previous simulations or experiments), the analytical solution provided by Eq. 16 can simplify the computations and the numerical solution of Eq. 1. For each  $x$  and time combination, the corresponding temperature is easily computed.

### 3.4 Temporal evolution of species concentration inside the HC catalytic converter, detailed simulations



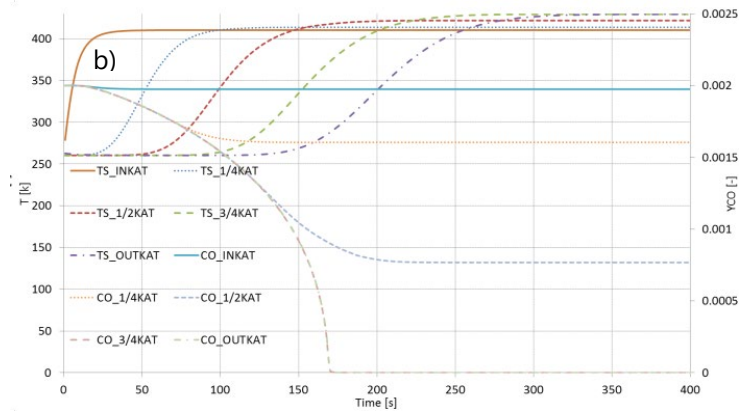


Fig. 6. Solid temperature and CO mass concentration in time at different catalytic converter space positions with  $T_s(t=0)=260\text{K}$ ,  $\dot{m}_F=0.0043\text{kg/s}$  and  $T_{Fin}=390\text{K}$  (a) and  $T_{Fin}=410\text{K}$  (b).

Most of the emissions of a vehicle are produced during the first seconds, when the catalytic converter has still not reached the minimum temperature for reactions to happen. The measurements and simulations performed in our laboratory on a Euro6 gasoline vehicle have shown that 17% of the CO, 91% of the THC and 66% of the NO<sub>x</sub> emissions during the WLTC cycle happen in the first 300 s after the engine cold start (20°C).

Fig. 6 describes both temperature and mass CO concentrations in time at the already described five different space positions along the catalytic converter.  $T_s(t=0s)=260\text{K}$ ,  $\dot{m}_F=0.0043\text{kg/s}$  and  $T_{Fin}=390\text{K}$  in (a) while  $T_{Fin}=410\text{K}$  in (b). The dependence of CO concentration from the evolving (increasing) solid temperature is evident. Independently of  $T_{Fin}$ , reactions start only slightly before 20s when  $T_s$  reaches circa 385K. The first oxidation reactions can be evidenced slightly before  $t=20\text{s}$ , where the CO concentration in the first quarter of the catalytic converter starts decreasing, falling below the CO concentration in the inlet. The CO concentration in the remaining catalyst parts (all along  $t<80\text{s}$ ) is identical with the CO concentration in the first quarter, evidencing that no reactions happen in the downstream catalyst parts yet. This is consistent with the low temperature at these parts. At about  $t=80\text{s}$  the temperature in the first quarter of the catalytic converter stabilizes, and the reaction rate of CO oxidation stabilizes as well, while, consequently, the CO concentration (at  $x=1/4L$ ) remains constant. The further decrease of the CO concentration in the next quarter of the catalytic converter evidences the onset of the reactions here. The reaction rate in the second quarter is slightly higher due to the slightly higher temperature, consequence both of convection heat transfer and exothermic heat released by the reactions happening in the first quarter. In the same way, around 130s, in the entire first half of the catalytic converter, solid temperature, reaction rate and CO concentration have reached constant levels and reactions start in the third quarter.

In the first case with  $T_{Fin}=390\text{K}$ , the conversion remains incomplete, CO is exiting the catalytic converter while the temperatures and the reaction rates are almost homogeneously distributed along the catalytic converter. On the contrary, at  $T_{Fin}=410\text{K}$ , the conversion is complete: the final temperature and the reaction rates increase along the catalytic converter and all the oxidation happens in the first three catalyst quarters.

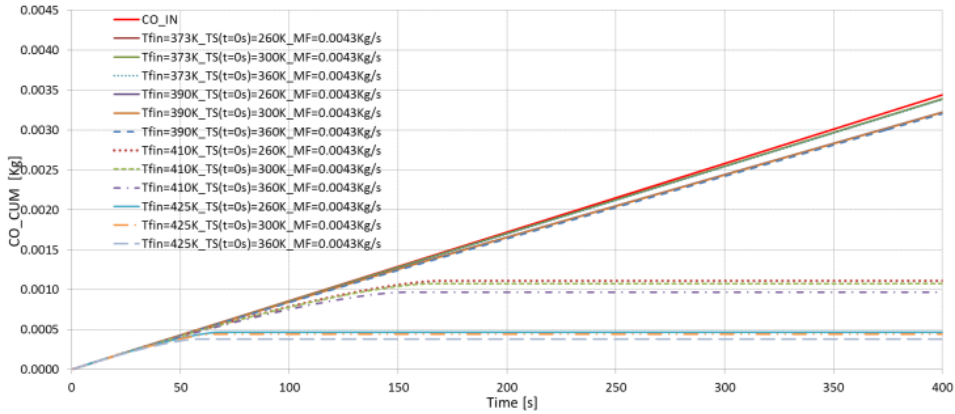


Fig. 7. CO cumulative emissions in time with  $T_S(t=0)=(260, 300, 360)K$ ,  $\dot{m}_F = 0.0043\text{kg/s}$  and  $T_{Fin}=(373, 390, 410, 425)K$ .

Cumulative emissions are reported in Fig. 7 for the different configurations examined. In addition, the cumulative CO exiting the engine and entering the catalytic converter is reported (solid red line). Independently of  $T_{Fin}$  and  $T_{S0}$ , for the first 30s no reactions are happening and CO emissions consist of the linear accumulation of the CO flowing in and out the catalytic converter. First deviations from the linear accumulation can be observed for the  $T_{Fin}=425K$  and  $T_{S0}=360K$  case (highest fluid and solid initial temperatures). Later in time, reactions start in configurations with descending  $T_{Fin}$ . The most evident differences are noticed between cumulative emissions in the case of  $T_{Fin}=390K$  and of  $T_{Fin}=410K$ . For the case with  $T_{Fin}=425K$ , already after 50s CO is fully oxidized, while only after 150s when  $T_{Fin}=410K$ . The full conversion is not reached in the case of  $T_{Fin}=390K$  or  $T_{Fin}=373K$ . Considering the different  $T_{S0}$ , the effect of higher  $T_{S0}$  reaches almost 30% in more conversion in the case of  $T_{Fin} = 425K$ .

With the developed analytical approach for the initial catalyst heat-up phase, as shown in Section 3.4, it is possible to compute also the emissions before any reactions start in a straightforward analytical manner. However, as soon as reactions release significant amounts of heat, the temperature increases and this in turn increases reaction rates in an exponential manner (Langmuir-Hinshelwood, Eq. 10). Here any further solution without solving the differential equations is only a very crude approximation.

### 3.5 Reciprocal influence of the different pollutants and the related reaction mechanisms, simulations with Axisuite

Detailed simulations taking into account the reaction mechanisms of further pollutants and their mutual interactions required large amount of CPU time. Therefore a different approach was adopted based on the tailored simulation commercial package, Axisuite. Analyzing the mutual interactions of the most important reactions requires the inclusion of all major pollutants (i.e. CO, NO<sub>x</sub> and HCs). This occurs only in TWC applications.

The aim of this section is to reproduce with Axisuite the cases analyzed with detailed simulations in the previous sections, in order to point out the importance of the interaction of the involved chemical mechanisms, incorporating the entire derived reaction scheme as shown in Table 3. All simulations have been performed based on the identical standard case as the results presented in the previous sections: Exhaust gas of constant temperature  $T_{Fin}(x=0)$  and mass flow rate  $\dot{m}_F$  flowing in a catalytic converter with an initial, lower and uniform temperature  $T_S(t=0) = T_{S0}$ . Moreover, the influence of varying inlet  $\dot{m}_F$ ,  $T_{Fin}$ ,  $T_{S0}$  is studied.

Focusing on a TWC application and near stoichiometric gas compositions, it was decided to choose two real exhaust gas compositions, one slightly lean, the other slightly rich as shown in Tables 4-5. The corresponding  $\lambda$  was computed according to Brettschneider equation [14][15]:

$$\lambda = \frac{[CO_2] + \left[\frac{CO}{2}\right] + [O_2] + \left[\frac{NO}{2}\right] + \left(\frac{H_{CV}}{2} \cdot \frac{3.5}{3.5 + \frac{[CO]}{[CO_2]}}\right) - \frac{O_{CV}}{2} \cdot ([CO_2] + [CO])}{\left(1 + \frac{H_{CV}}{4} - \frac{O_{CV}}{2}\right) \cdot ([CO_2] + [CO]) + (n \cdot [HC])} \quad (18)$$

Where  $H_{CV}$ ,  $O_{CV}$  and  $n$  are respectively the number of atoms of H, O and C in the fuel. The last term in the nominator of the Brettschneider equation is an empirical estimation of water (in general not measured) in the exhaust gas.

Table 4: Lean mixture molar species concentrations at the catalyst entrance.

CO	CO <sub>2</sub>	NO	C <sub>3</sub> H <sub>6</sub>	O <sub>2</sub>	H <sub>2</sub> O	N <sub>2</sub>	$\lambda$
0.00266	0.124	0.00168	0.00384	0.00772	0.14	0.72	1.024

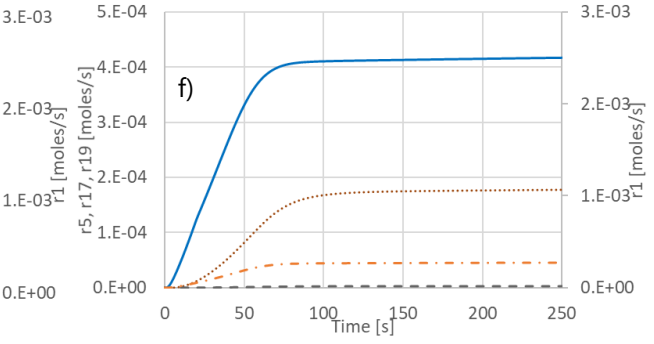
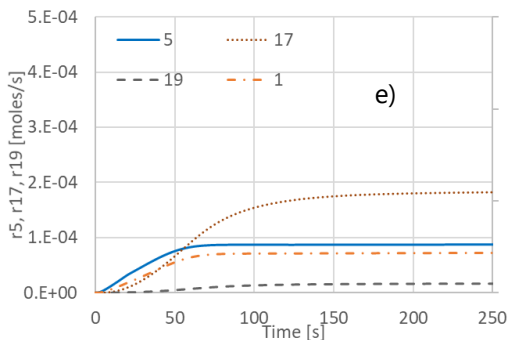
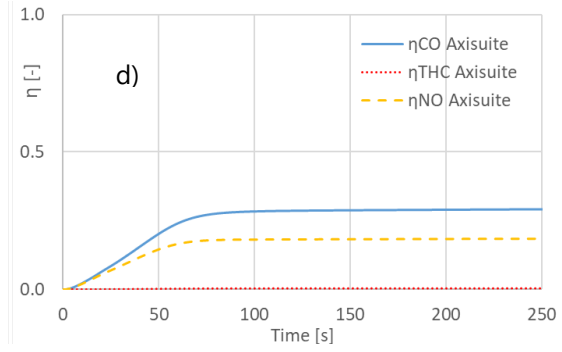
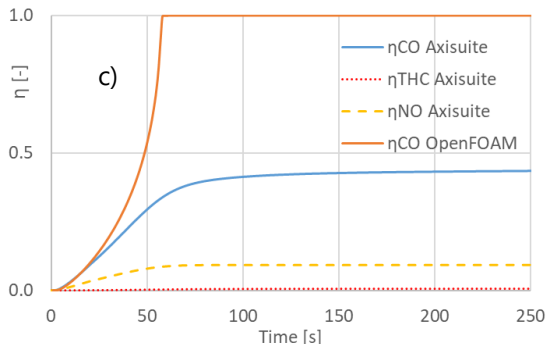
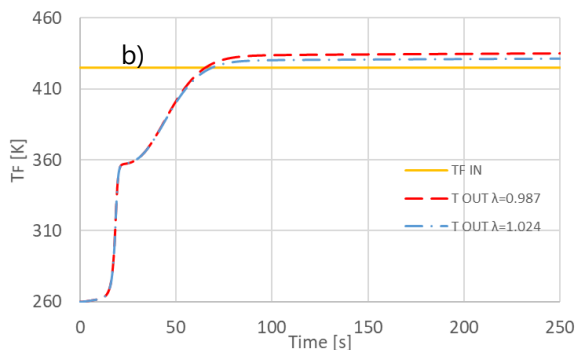
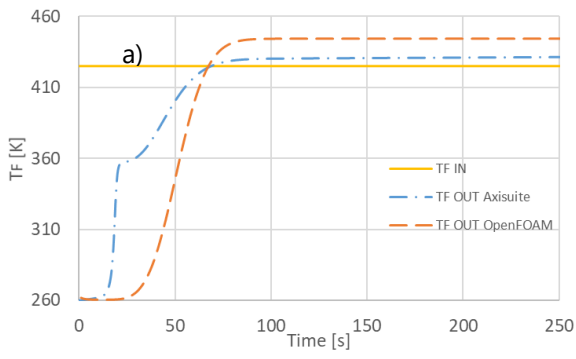
Table 5: Rich mixture species molar concentrations at the catalyst entrance.

CO	CO <sub>2</sub>	NO	C <sub>3</sub> H <sub>6</sub>	O <sub>2</sub>	H <sub>2</sub> O	N <sub>2</sub>	$\lambda$
0.00493	0.120639	0.003909	0.001305	0.005544	0.142068	0.722474	0.987

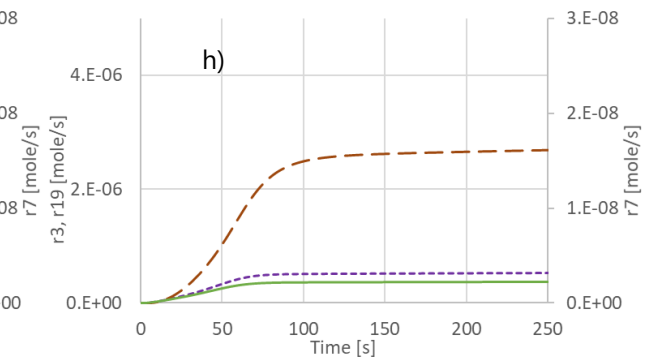
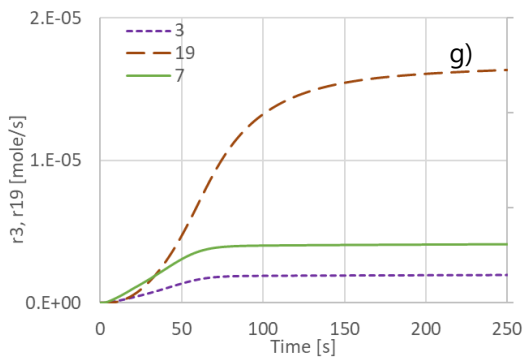
After some preliminary considerations, the set of different configurations analyzed with the above listed exhaust gas compositions are listed in Table 6. The base case is evidenced in bold (#3).

Table 6. Simulations parameters matrix.

Case #	$\lambda$	$\dot{m}_F$ [kg/s]	Corresponding $v_F$ [m/s]	$T_{Fin}$ [K]	$T_{S0}$ [K]
1	1.024	0.0043	0.3	410	260
2	1.024	0.0172	1.25	410	260
<b>3</b>	1.024	<b>0.0172</b>	<b>1.25</b>	<b>425</b>	<b>260</b>
4	1.024	0.0172	1.25	425	360
5	0.987	0.0043	0.3	410	260
6	0.987	0.0172	1.25	410	260
7	0.987	0.0172	1.25	425	260
8	0.987	0.0172	1.25	425	360

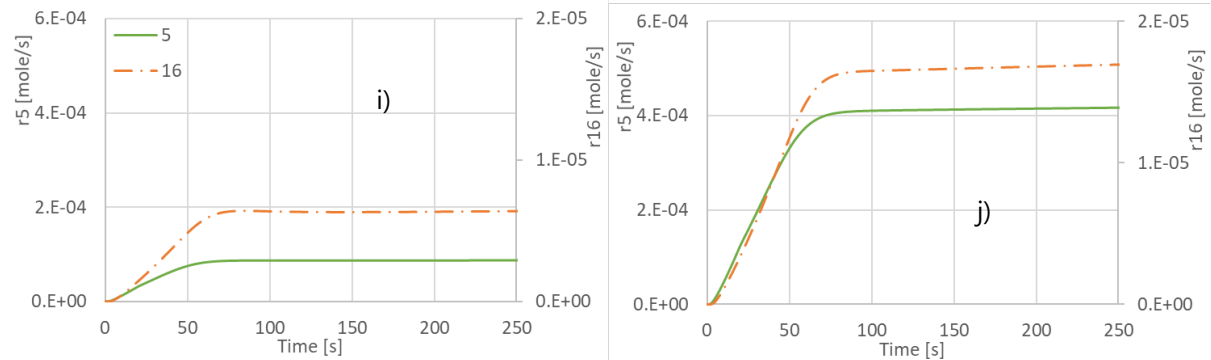


#	Reactions
5	$\text{CO} + \text{NO} \rightarrow \text{CO}_2 + 1/2 \text{N}_2$
17	$2 \text{sCeO}_2 + \text{CO} \rightarrow \text{sCe}_2\text{O}_3 + \text{CO}_2$
19	$2 \text{sCeO}_2 + 1/6 \text{C}_3\text{H}_6 \rightarrow \text{sCe}_2\text{O}_3 + 1/2 \text{CO} + 1/2 \text{H}_2\text{O}$
1	$\text{CO} + 1/2 \text{O}_2 \rightarrow \text{CO}_2$



#	Reactions
---	-----------

3	$C_3H_6 + 9/2 O_2 \rightarrow 3 CO_2 + 3 H_2O$
19	$2 sCeO_2 + 1/6 C_3H_6 \rightarrow sCe_2O_3 + 1/2 CO + 1/2 H_2O$
7	$C_3H_6 + 3 H_2O \rightarrow 3 CO + 6 H_2$



#	Reaction
5	$CO + NO \rightarrow CO_2 + 1/2 N_2$
16	$sCe_2O_3 + NO \rightarrow 2 sCeO_2 + 1/2 N_2$

Fig. 8. Comparison between cases #3 and #7 of Table 6, thus between slightly lean (a, c, e, g, i) and slightly rich (b, d, f, h, j) mixtures in terms of fluid temperatures (a,b), conversion efficiencies  $\eta_{CO}$ ,  $\eta_{THC}$ ,  $\eta_{NO}$  (c, d), most significant chemical reactions related to CO conversion (e,f), most significant chemical reactions related to THC conversion (g,h), and most significant chemical reactions related to NO conversion (i,j) ( $\dot{m}_F=0.0172\text{kg/s}$ ,  $T_{Fin}=425\text{K}$ ,  $T_{S0}=260\text{K}$ ).

In Fig. 8a, c the temperature and CO concentrations evolution over time are compared as computed either by the detailed OpenFOAM simulations (taking into account only CO oxidation) or by the Axisuite simulations taking into account all related pollutant reactions. The differences are striking. In the latter case:

- The temperature increase in the catalyst during the initial transient phase is faster.
- The final temperature reached in the stationary phase is lower.
- The first realizable CO oxidation starts almost at the same time (in spite the faster warm up).
- The CO oxidation reached at the stationary phase is significant lower (18% vs 100%).

The involved chemical reactions, as shown in Fig. 8 e-g-h-i, provide some interesting insights. The reactions starting almost immediately after the start are reactions 5, 16 and 7, i.e. the NO<sub>x</sub> reduction with CO and Ce<sub>2</sub>O<sub>3</sub> as well as the steam reforming of C<sub>3</sub>H<sub>6</sub>. While reaction 5 consumed CO, reaction 7 produces CO. However, reaction 7 produces also H<sub>2</sub>, which is subsequently oxidized according to reaction 2 (not shown in Fig. 8, but in Table 3). Now, hydrogen oxidation results in H<sub>2</sub>O with significant heat release, having a major contribution in the catalyst heat-up. Although the catalyst initial heat-up is faster, it is levelling off very soon, while temperatures are only moderate. So, the reaction rates remain modest (for the CO and NO<sub>x</sub> reactions) and very low for the C<sub>3</sub>H<sub>6</sub> related reactions. It is clear from Fig 8c that the CO oxidation is much stronger when it is the only reaction taken into account and significantly weaker when also the other pollutant reactions occur simultaneously on the identical active sites.

Given the modest temperatures reached in the stationary phase, the NO<sub>x</sub> reduction is also modest, while the C<sub>3</sub>H<sub>6</sub> oxidation very small, Fig. 8c. It is well known [7] that CO occupies the active sites and inhibits the oxidation of further hydrocarbons as long as present in abundance. Very similar are the conversion reached with a slightly rich mixture, Fig. 8d: at almost equal temperatures (Fig. 8b) and with less oxygen

available NO<sub>x</sub> reduction reaches a higher level, while CO oxidation a lower. C<sub>3</sub>H<sub>6</sub> oxidation is, as expected, very low.

Figs. 8e-j provide a good overview of the main reactions mechanisms involved at this low temperature level. The following summarized results refer to the stationary state. For the CO abatement (in lean and rich mixture, Figs 8e-f):

- The main mechanism is direct oxidation.
- Reaction with NO is somehow half an order of magnitude weaker.
- Ceria catalyzed oxidation is somehow an order of magnitude weaker.
- Almost of the same order of magnitude is CO produced by ceria catalyzed C<sub>3</sub>H<sub>6</sub> partial oxidation.

The weak, but not completely inexistent, C<sub>3</sub>H<sub>6</sub> abatement is more pronounced in the lean and less in the rich mixture as a result of (Figs 8g-h):

- Direct oxidation
- Ceria catalyzed C<sub>3</sub>H<sub>6</sub> partial oxidation (an order of magnitude weaker in respect to direct oxidation).
- C<sub>3</sub>H<sub>6</sub> steam reforming, being even two orders of magnitude weaker, but playing an essential role in the catalyst heat-up as it produces H<sub>2</sub>, which oxidizes to water under substantial heat release, aiding the heat-up.

NO<sub>x</sub> reduction at these low temperatures is (Figs. 8i-j):

- Mainly due to the reduction through CO
- Catalytic reduction on ceria sites (about one order of magnitude weaker)

A subset of the results of the simulations with the different parameters of Table 6 is shown in Figs. 9 and 10, while the entire results are summarized in terms of the cumulative emissions over the first 250s in Table 7.

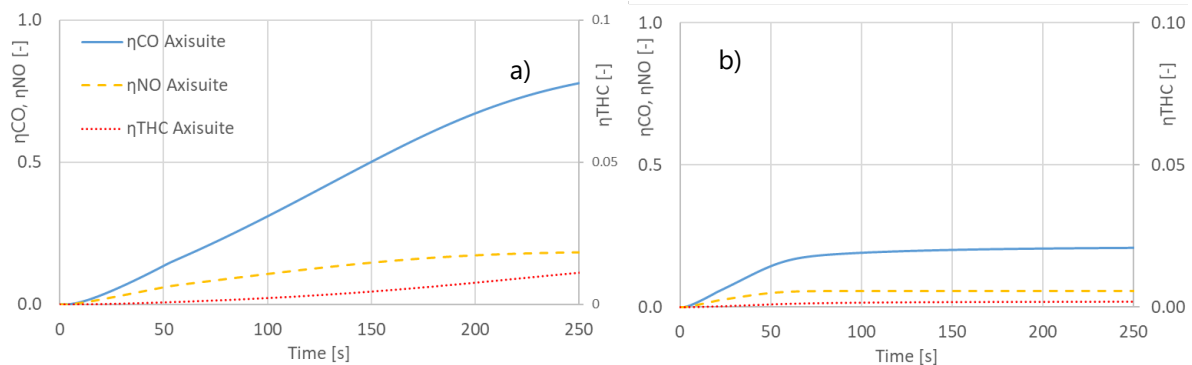


Fig. 9. Comparison between cases #1 and #2 (lean mixture) of Table 6 in terms of conversions efficiency,  $\dot{m}_F=0.0043\text{kg/s}$  (a) and of  $\dot{m}_F=0.0172\text{kg/s}$  (b). ( $T_{Fin}=410\text{K}$ ,  $T_{S0}=260\text{K}$ ).

Keeping all parameters constant and increasing fourfold only the mass flow results in faster heat up. As the pollutant concentration is constant, the mass of the fluid entering the catalyst increases also by four times. The reaction rates though are not increasing in the same manner, thus, the efficiency of the catalyst decreases in Fig. 9 (cases #1, #2 of Table 6), and the cumulative emissions increase by more than four times, see Table 7 (cases #1, #2 and #5, #6 of Table 6). Since the mixture is slightly lean, CO oxidation is preminent, while some weak C<sub>3</sub>H<sub>6</sub> oxidation can also be seen.

The effect of different in-flowing gas temperatures is shown in Fig. 10, this time with a rich mixture. The NO<sub>x</sub> reduction prevails, while no C<sub>3</sub>H<sub>6</sub> oxidation is evident. The effect of the higher inflow temperature is clear, however in terms of cumulative emissions (Table 7 cases #5, #6 and #2, #3), it is rather modest.

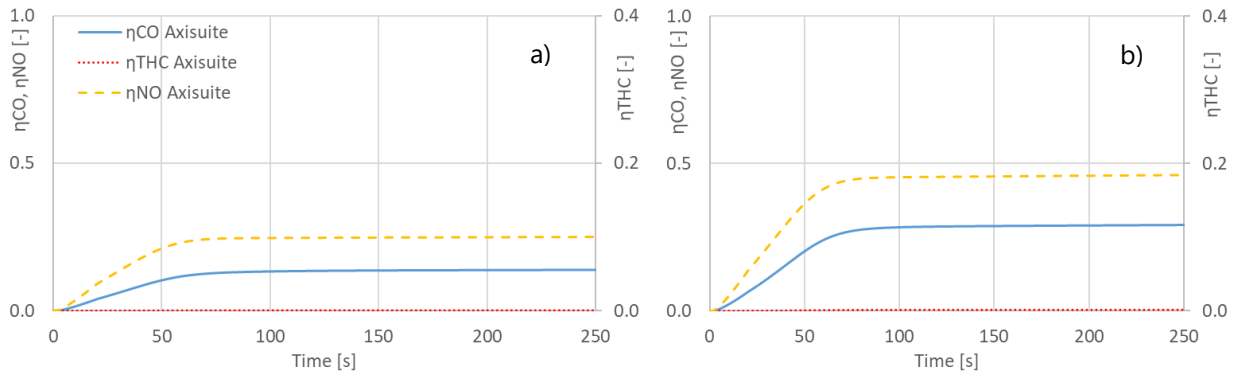


Fig. 10. Comparison between cases #6 and #7 (rich mixture) of Table 6 in terms of conversion efficiency with  $T_{Fin}=410K$  (a) and  $T_{Fin}=425K$  (b) ( $\dot{m}_F=0.0172kg/s$  (b).  $T_{S0}=260K$ ).

Table 7. Cumulative emissions in [g] during 250s of converter operations for different operating conditions.

Case #	cumCO [g]	cumTHC [g]	cumNO [g]
1	1.67	2.01	1.68
2	9.27	8.07	7.20
3	7.16	8.04	6.96
4	6.84	8.04	6.93
5	3.34	0.69	3.30
6	18.4	2.75	16.1
7	15.7	2.74	14.9
8	15.3	2.74	14.7

### 3.6 Additive Manufactured (AM) catalytic converters, detailed simulations

The analysis conducted in [16] for HC converters, has been setup for Additive Manufactured (AM) open cell polyhedral cubic cell catalytic converters. In the first place to mention is, that, to our knowledge so far, there exists no commercial software for the simulation of AM structures. Therefore the detailed simulations approach was chosen taking in to account the CO oxidation only. The aim was to study basic aspects of heat and mass transfer including a simple reaction mechanism during cold starts and produce a sound basis for comparing with conventional Honeycomb catalysts.

While the approach is very similar as for honeycombs (Sections 4.1-4.4) the simulation technology is completely different, based on more complex algorithms. The flow inside a honeycomb channel is laminar, in contrast to the flow through the tortuous AM structures is constantly changing direction with varying degrees of turbulence. The methodology and the results are reported in detail in [17]. The AM geometries considered are described in Section 3.1. The heat up of these Additive Manufactured (AM) catalytic substrates during cold start has been analyzed using numerical simulation and analytical methods. The focus was set on the temporal and spatial profiles of the temperature and CO concentration

inside and at the exit of the converter. Moreover, the ranges of variability for the characteristics dimensions have been:  $T_{S0}=[260-360]K$ ,  $T_{Fin}=[410-425]K$  and  $\dot{m}_F=[0.0086-0.0344]kg/s$ .

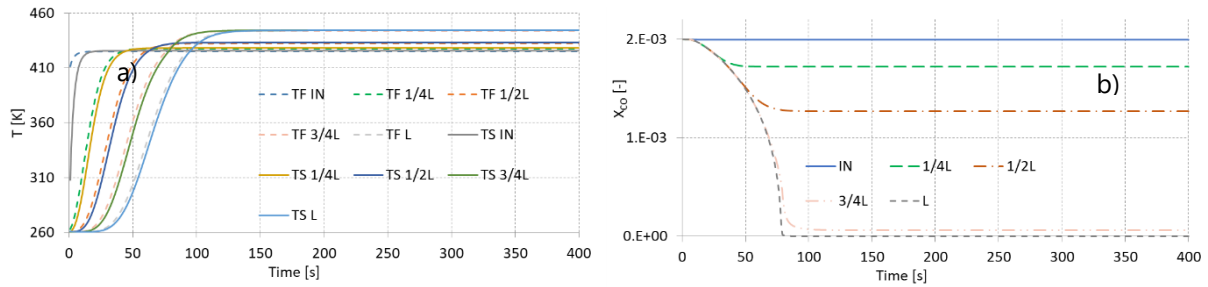


Fig. 11. Typical cold start of AM1 catalytic converter in terms of: (a) Fluid  $T_F$  (dashed lines) and solid  $T_S$  (solid lines) temperature time histories and (b) CO concentrations time histories at different locations inside the converter (IN, 1/4L, 1/2L, 3/4K, L). The simulation is characterized by  $T_{Fin}=425K$ ,  $T_{S0}= 260K$  and  $\dot{m}_F=0.0172kg/s$ .

Fig. 11 presents a typical AM heat up process in terms of  $T_F$  and  $T_S$  time histories and CO concentrations at different local positions inside the converter. The results correspond to the case of AM1,  $T_{Fin}=425K$ ,  $T_{S0}=260K$  and  $\dot{m}_F=0.0172kg/s$ . Dashed lines represent  $T_F$ , while solid lines  $T_S$  (catalytic converter). Observations that can be derived from Fig. 11 are still valid, with some specifications, for different combinations in terms of  $T_{S0}$ ,  $T_{Fin}$  and  $\dot{m}_F$ . The heat up process during the first 400s operations of a converter with AM open foam geometry is very similar to the one with HC geometry (see Section 4.1-4.4).

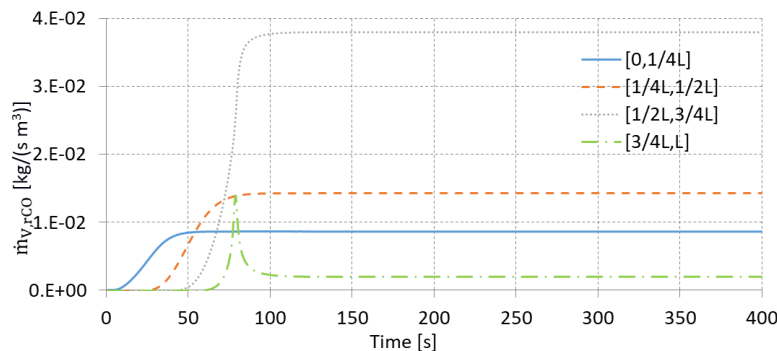


Fig. 12. Reacting CO mass rates,  $\dot{m}_{V,RCO}$ , in the selected locations ( $T_{Fin}=425K$ ,  $T_{S0}=260K$  and  $\dot{m}_F=0.0172kg/s$ ).

Fig. 12 represents the CO mass flow reacted  $\dot{m}_{V,RCO}$  in each of the catalyst quarters under consideration. For  $t < 7s$  no reactions are evident. Thereafter initial reactions start at the entrance of the first quarter and equilibrium is reached at around  $t=42$ secs. Reactions in the second quarter start later, stabilizing at a slightly higher reaction rate. The reaction rate in the third quarter is the highest, while the remaining CO in the last quarter is very low, leading to lowest  $\dot{m}_{V,RCO}$  there. In the last quarter, only a peak is evidenced at  $t=75$ secs. At this time the reactions in the third quarter have not reached the highest rate yet, thus allowing some more CO slip to the last quarter. After  $\dot{m}_{V,RCO}$  in the third quarter stabilizes at a high value ( $3.8 \cdot 10^{-2} kg/(sm^3)$ ), only a low amount of CO reaches the fourth quarter and reacts there.

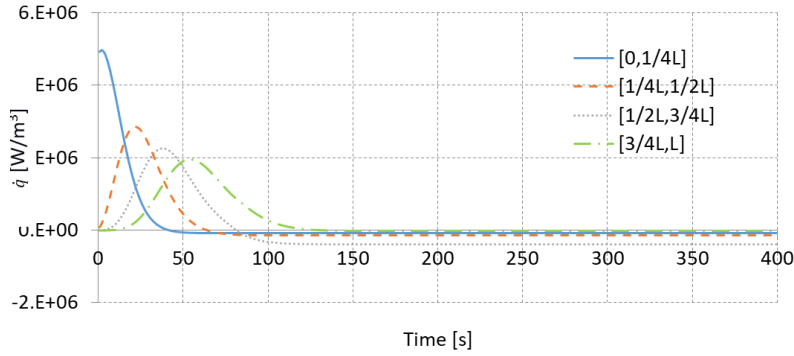


Fig. 13. Heat exchanged from the fluid to the solid,  $\dot{q}$ , integrated over intervals of the catalytic converter between the selected locations ( $T_{Fin}=425K$  and  $\dot{m}_F=0.0172kg/s$ ,  $T_{S0}=260K$ ).

These observations are also reflected in  $\dot{q}$  transferred from the fluid to the solid, as shown in Fig. 13. From upstream to downstream, each catalyst quarter experiences the initial heat-up phase, where the solid is heated up by the gases (positive  $\dot{q}$ ). Also first chemical reactions start, their influence however is weak. With time the solid heats up and resumes the temperature of the entering gases. The second heat up phase begins, the heat released by the stronger chemical reactions leads to higher temperatures of the solid, the heat flow reverses (negative and much lower) from the solid to the fluid.

For the initial temperature differences chosen here, the convective heat flux in the initial warm-up phase, as shown in Fig. 13, is significantly larger in respect to the heat released by the chemical reactions in the second phase. The peak of the heat flux in the initial warm-up phase is highest in the catalytic converter entrance and declines in the downstream. This is explained taking into account the temporal and local evolution of the temperatures (Fig. 11); the temperature gradients decline with time and space (downstream). The declining temperature gradients, however, result in (temporal) slower heat up. Thus, the duration of the initial heat-up phase increases in the downstream parts. Table 8 summarizes the duration of the initial heat up phase as well as the energy exchanged in this phase.  $\dot{q}$  in the first phase is almost evenly distributed in the four parts of the catalytic converter under consideration. The subsequent energy released by the chemical reactions (convected back to the fluid and a smaller part conducted within the solid) is also shown in the Table 8. For obtaining comparable values of energy in the two phases, for each quarter, the time span used in the second phase is equal to the one characteristic of the first one.

Table 8: Duration and value of heat exchanged during the initial heat-up phase (from fluid to solid) in comparison to the heat released by the chemical reactions in the second phase (assuming identical duration of both phases). The energy released by the chemical reactions in the last quarter is not reported because of the very small amount of CO left from the preceding quarters, allowing no direct comparison.

Catalyst part	Duration of the initial phase, heat from fluid to solid [s]	Heat exchanged (initial phase from fluid to solid) $q$ [kJ/m <sup>3</sup> ]	Heat released by the chemical reactions in the second phase $q$ [kJ/m <sup>3</sup> ]
[0,1/4L]	41	$8 \cdot 10^4$	$3.17 \cdot 10^3$
[1/4L, 1/2L]	64	$8.48 \cdot 10^4$	$8.33 \cdot 10^3$
[1/2L, 3/4L]	85	$8.51 \cdot 10^4$	$3.04 \cdot 10^4$
[3/4L, L]	130	$9.25 \cdot 10^4$	

The dimensionless approach adopted for the investigation of the thermal behavior of HC catalytic converters is also implemented for the AM catalytic converters. The same conclusions derived for HCs are valid for AM converters: the introduction of dimensionless temperature differences, dimensionless time and dimensionless space coordinates (Eqs. 3-6) evidences the similarity of all examined cases (i.e. for

different mass flow rates, inlet flow and catalytic converter initial temperatures as well as lengths). Moreover, the AM catalytic converters heat up in dimensionless parameters has the same characteristic S-type shape already found for HC converters, which is a double logarithmic function that can be approximated by the corresponding analytical expression (already derived in Section 4.3, Eq. 16, see Fig. 14).

Fig. 14 describes the dimensionless temperature response of AM1,  $\theta_F$ , as a function of the dimensionless time-space coordinate  $\tau/\xi$ . Different lines correspond to different conditions, i.e.  $T_S(t=0)=[260,360]$ K,  $T_{Fin}=[410,425]$ K and  $\dot{m}_F=[0.0086,0.0172]$ kg/s, and to different catalytic converter lengths (1/2L and L). The initial  $\theta(T_S=T_S(t=0)=T_0)=0$  and approaches unity ( $T_S=T_{Fin}$ ) at the end of the initial heat-up phase. Values higher than 1 correspond to the second phase of the warm up and are results of heat released by the reactions.

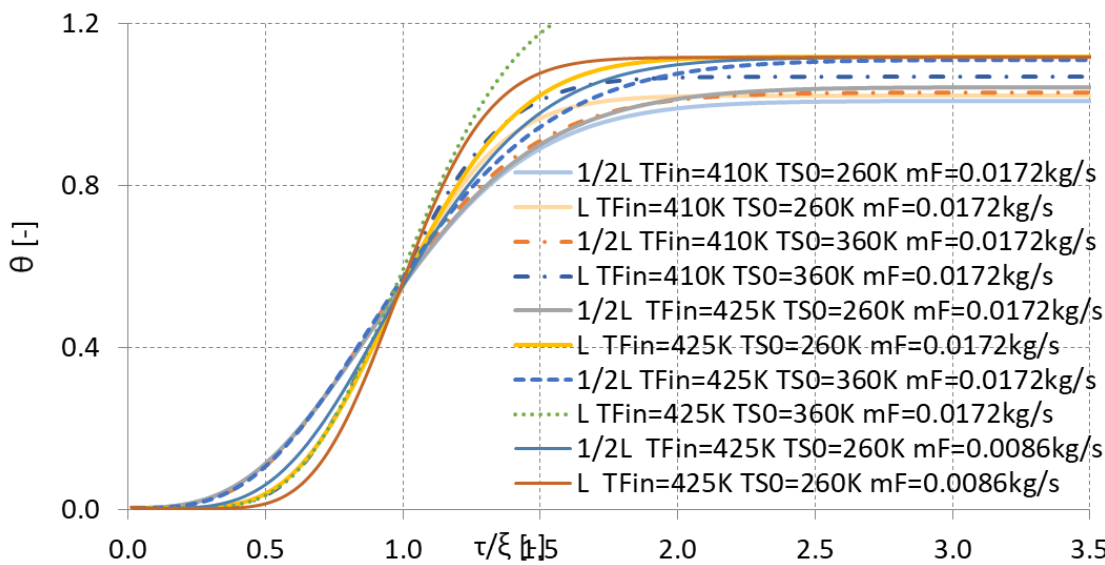


Fig. 14.  $\theta_F$  in function of  $\tau/\xi$ , with varying  $T_S(t=0)=[260,360]$ K,  $T_{Fin}=[410,425]$ K,  $\dot{m}_F=[0.0086,0.0172]$ Kg/s and  $x=[1/2L,L]$ .

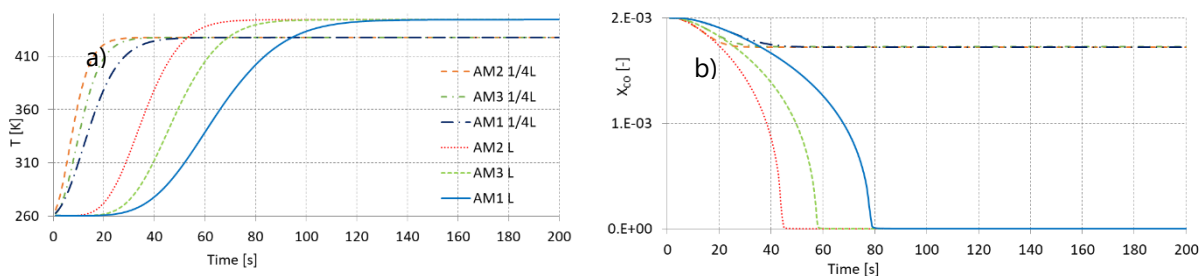


Fig. 15. Comparison of three different AM structures (see Table 2) in terms of  $T_F$  (a) and  $X_{CO}$  (b) time histories in different locations (1/4L, L) ( $T_{Fin}=425$ K,  $T_{S0}=260$ K and  $\dot{m}_F=0.0172$ kg/s).

Three AM converter substrates with different geometrical characteristics, thus different thermal and mechanical properties and different mass, have been compared in terms of thermal and conversion characteristics.

Fig. 15 compares the time evolution of  $T_F$  (a) and  $X_{CO}$  (b) for the three different structures (as described in Fig. 11 for AM1). Displayed are the time histories at the positions  $x=1/4L$  and  $x=L$ . The results correspond to the case of  $T_{Fin}=425$ K,  $T_{S0}=260$ K and  $\dot{m}_F=0.0172$ kg/s. On the whole, the warm up is similar among the different cases examined and the mechanism is the one already described in detailed before. However, the heat up characteristics in terms of rates and durations differ among the AM structures. AM2 shows the fastest heat up and the steepest temperature increase. This is valid in the initial heat-up

phase, when the catalytic converter is heated up by the fluid. AM2 is followed by AM3, while AM1 is the structure with the slowest heat-up characteristic.

Though this behavior may be puzzling, it can be well explained with some basic reasoning. During the initial heat-up phase, heat is transferred from the fluid to the solid. The heat transferred in a time step is proportional to

$$Q_{F \rightarrow S} \propto (h \cdot S_W \cdot \Delta T_F) \quad (19)$$

The heat transfer coefficient,  $h$ , is given by

$$h = \frac{Nu\lambda}{d_s} \quad (20)$$

Assuming that the heat and mass transfer analogy holds, then the Nusselt number's dependency on the strut diameter  $d_s$  must be similar to the Sherwood number's dependency on  $d_s$  according to [3]:

$$Nu = f(d_s^{0.3}) \text{ just as } Sh = f(d_s^{0.3}) \quad (21)$$

Thus  $h = f(d_s^{-0.7})$ , so that  $h_{AM3} = h_{AM2} = 1.39 h_{AM1}$ .

The surface, corresponding to  $S_W$ , on the other hand, is  $S_{W,AM3} = 1.43S_{W,AM2}$  and  $S_{W,AM1} = 1.22S_{W,AM2}$  based on the values reported in Table 2. This gives a rough estimation of the ratio of the heat transferred from the fluid to the solid among the three structures during one time step:

$$Q_{F \rightarrow S,AM3} = 1.43Q_{F \rightarrow S,AM2} \quad (22) \text{ and}$$

$$Q_{F \rightarrow S,AM2} = 1.14Q_{F \rightarrow S,AM1} \quad (23)$$

So the heat transferred from the fluid to the solid in one time step, assuming similar temperature gradients (for the beginning of the heat-up process at least is an acceptable assumption) is highest for AM3, followed by AM2 and then AM1. This amount of heat increases the internal energy of the solid (when neglecting the anyhow low conduction in the solid):

$$Q_{F \rightarrow S} = m_S c_v \left( \frac{dT_s}{dt} \right)_{AM} \quad (24)$$

Considering that the mass of each catalytic converter is a function of its porosity:  $m_S = m_{AM} = (1 - \varepsilon)V \cdot \rho$ , values from Table 2 give:  $m_{AM3} = 1.5m_{AM2}$  and  $m_{AM1} = 2m_{AM2}$  this simplified estimation yields:

$$\left( \frac{dT}{dt} \right)_{AM2} \sim 1.05 \left( \frac{dT_s}{dt} \right)_{AM3} \quad (25)$$

and

$$\left( \frac{dT}{dt} \right)_{AM2} \sim 1.75 \left( \frac{dT_s}{dt} \right)_{AM1} \quad (26)$$

The characteristics in Fig. 15 reflect quite well the approximations in Eqs. 25-26 since AM2 heats up first, followed by AM3 and then by AM1 (substantially later). Thus, on the surface of AM2, the initial chemical reactions start first and the 2<sup>nd</sup> heat-up phase, initiates earlier. Later in time the three structures end-up with identical temperature of 444K. This is clear, given that with all three structures full CO oxidation is reached (thus same reaction heat released).

### 3.7 Evaluation of Cold Start Emission Mitigation Strategies through external heating, detailed simulations

The aftertreatment system should be designed in order to optimize its heat up phase and to reach optimal operating conditions in minimal time. The most efficient way would be heating applied such that only the catalytic active sites are kept slightly above the light off temperature of the pollutants in question. There are different concepts in order to approach this idea in reality. Here, the two most discussed heating strategies are compared:

- 1) Additional heating the exhaust gas before the entrance of the catalyst, leading to higher temperatures for the fluid, and
- 2) Additional heating the catalyst (solid) itself.

The former can happen with the help of an electrical resistance, such systems are already existing, also in limited serial application. The latter is based on microwave heating, as proposed in [18]. However, in both strategies the ubiquitous heat exchange between the solid and fluid has to be taken into account. Nevertheless, a possibility to use a combination of both strategies can also be envisaged.

In the present project, a comparison of the two strategies has been attempted based on detailed simulations, taking into account CO oxidation. The most appropriate comparison should take into account the additional amount of pollutant reduced in relation to the additional energy spent for the heating (of either the fluid or the solid) in respect to a base case without any additional heating.

The fluid temperature distribution in the converter at half of the length at  $t=20s$  for the case of  $T_{Fin}=410K$ ,  $T_{S0}=260K$  and  $\dot{m}_F=0.0043kg/s$  is presented in Fig. 16. This different heating strategies in comparison are:

1. base case without any heating,
2. heating the entire converter with a power source of 1000W for 100s,
3. heating only one quarter of the converter with a power source of 1000W for 100s,
4. heating the entire converter with a power source of 2000W for 100s,
5. heating only one quarter of the converter with a power source of 2000W for 100s,
6. heating the fluid such that it enters at 640K for 100s (640K corresponds to the case of 1000W provided to the fluid).

From the comparison, it is evident that:

- Heating the fluid before entering the catalyst results in a better heat up of the converter at the inflow. The gases though cool down towards the solid initial temperature already in the first quarter of the catalyst.
- Heating the solid part of the catalyst results in a rather modest increase of temperature in the entrance part; however, overall temperature increase is more uniform and it is higher after the first quarter.
- Heating only the upstream quarter of the converter results in even higher temperatures almost everywhere along the converter.

Fig. 17 compares the same six cases in terms of temperature and CO concentration time history at  $x=1/4L$  in  $0 < t < 100s$ . The same operating conditions are considered:  $T_{Fin}=410K$ ,  $T_{S0}=260K$  and  $\dot{m}_F=0.0043kg/s$ . The following considerations can be added:

1. With all the heating strategies, gases and solid are heated faster than without. As soon as the heating is switched off, the temperatures bounce back towards the temperatures without heating.
2. Considering the solid heating strategies: concentrating the heat in the first quarter is beneficial and allows to reach higher temperatures levels, thus higher CO oxidation.

- In all the cases where the solid is heated, higher temperatures at the start are reached for  $t < 36s$ . However, heating the fluid results in substantial higher temperature with respect to heating the entire solid thereafter for  $36s < t < 100s$  (see Fig. 17a).
- Accordingly, reactions are immediately initiated in the case where the fluid is heated, while (see Fig. 17b) heating the solid has a small delay. This delay is lower for strategies related to heating only the first converter quarter, while it is bigger for strategies related to heating the entire converter.
- After  $t = 100s$  when the heating is switched off, all the cases go back to a CO concentration equal to the one in the base case.

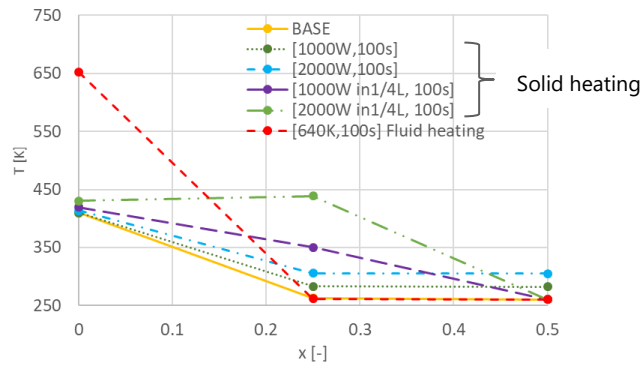


Fig. 16. Fluid temperature profile along the catalytic converter half length (indicated as fraction of L) at  $t = 20s$ ,  $T_{Fin} = 410K$  and  $T_s(t=0) = 260K$  and  $\dot{m}_F = 0.0043kg/s$ .

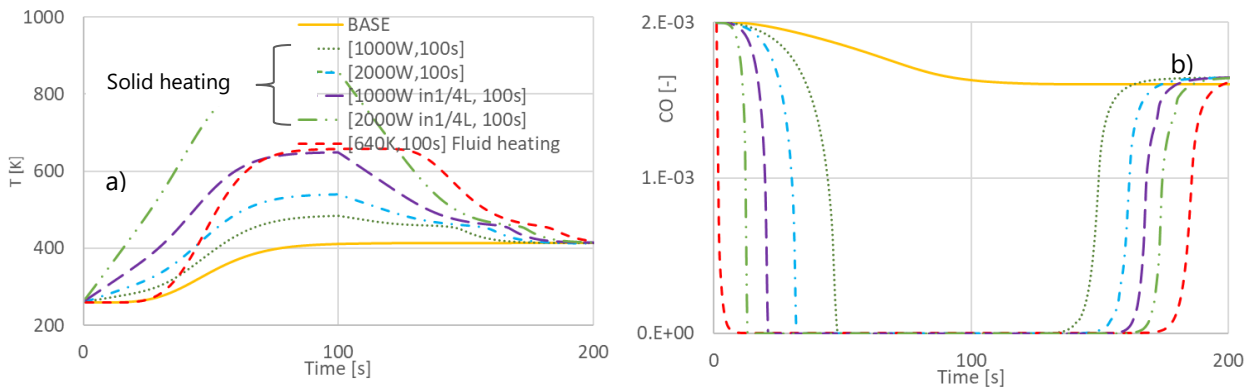
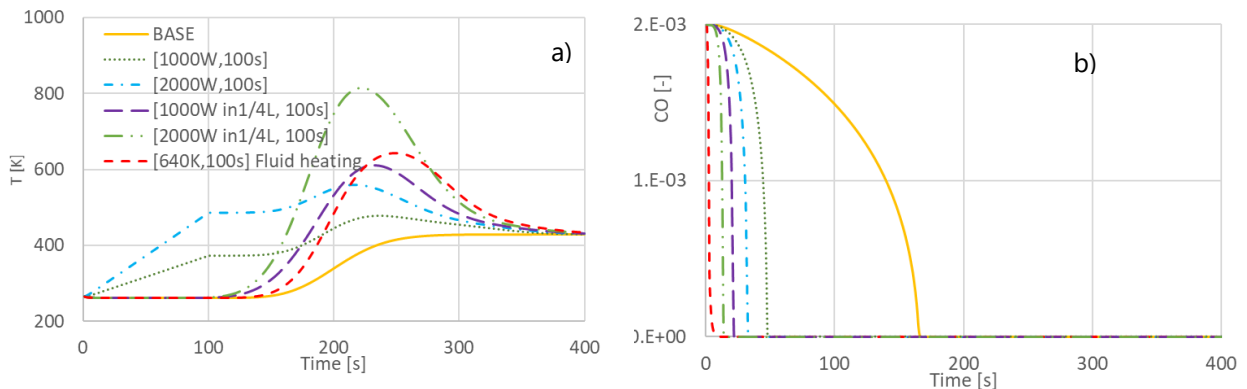


Fig. 17. Fluid temperature (a) and CO mass concentration (b) in time at  $x = 1/4L$  with  $T_{Fin} = 410K$ ,  $T_s(t=0) = 260K$ ,  $\dot{m}_F = 0.0043kg/s$ .



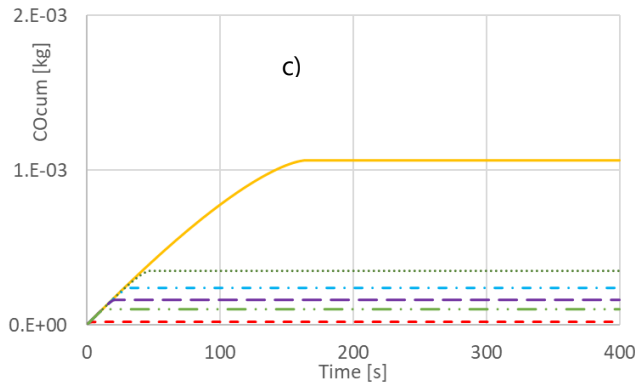


Fig. 18. Fluid temperature (a), CO mass concentration (b) and CO cumulative emissions (c) in time at at  $x=L$  with  $T_{Fin}=410K$ ,  $T_S(t=0)=260K$ ,  $\dot{m}_F=0.0043kg/s$ .

Fig. 18 analyzes the fluid conditions at the converter exit  $x=L$  in terms of temperature (a), CO mass concentration (b) and cumulative CO emissions (c). The same operating conditions are considered:  $T_{Fin}=410K$ ,  $T_{S0}=260K$  and  $\dot{m}_F=0.0043kg/s$ . Moreover, the comparison involves the identical six heating strategies of Figs. 16-17.

It is evident that:

- In all the cases considered, even the one without heating, full conversion (Fig. 18b) is reached inside the converter, although with different delays. Accelerating conversion, is most efficiently reached by heating the fluid upstream the converter.
- Heating the solid is only efficient when concentrating the energy input in the upstream quarter of the converter.
- During the initial heat up, for  $t < 150s$ , higher temperature is reached with heating the entire converter at 2000W, while for  $t > 150s$  higher temperature is reached when concentrating the heating only in the first converter quarter.

Already these results point towards the crucial criteria for the lay-out of an efficient catalyst heating strategy. The heat to be provided has to be such, that the light-off temperature of the pollutant in question is reached in the upstream catalyst part, initiating enough chemical reactions which in turn release enough heat, that is not entirely transferred to the flowing gases.

At  $T_{Fin}=410K$ ,  $T_{S0}=260K$  and  $\dot{m}_F=0.0043kg/s$ , the optimal strategy is heating the fluid before entering the converter. This consideration may change at higher  $\dot{m}_F$ .

Fig. 19 shows the temperature distribution along the converter at  $t=20s$  in the case of  $T_{Fin}=410K$  and  $T_S(t=0)=260K$  and a much higher  $\dot{m}_F=0.0344kg/s$ . Similar heating strategies as before are here considered:

- heating the entire converter for 50s with 2000W,
- heating the first quarter converter for 50s with 1000W,
- heating the first quarter converter for 50s with 2000W and
- heating the fluid for 50s with 2000W, thus the fluid enters the converter at  $T_{Fin}=468K$  for 50s.

Comparing Fig. 19 with Fig. 17, it is clear that:

- The same behavior seen for  $\dot{m}_F=0.043kg/s$  is here recognizable: in the first converter portion, higher temperatures can be achieved by heating the fluid, while in the second converter half, higher temperatures are reached when heating the entire converter.
- Higher  $\dot{m}_F$  allows a faster transient process which leads to an overall more uniform temperature distribution:
  - If heating the fluid, at the entrance of the converter, the fluid enters with a lower temperature with respect to the case at lower  $\dot{m}_F$ .

- Downstream the converter, in all the heating strategies examined, the faster flow allows to reach higher temperatures before in time.

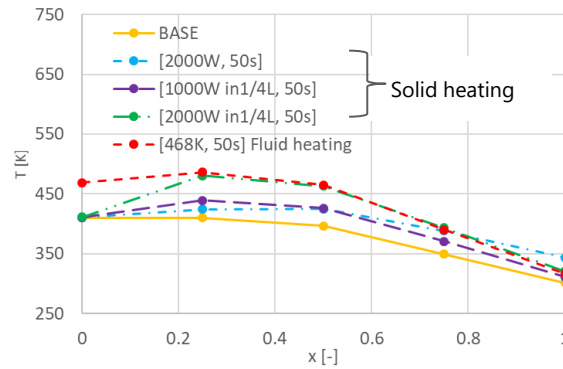


Fig. 19. Fluid temperature profile along the catalytic converter length (indicated as fraction of  $L$ ) at  $t=20s$ ,  $T_{Fin}=410K$  and  $T_s(t=0)=260K$  and  $\dot{m}_F=0.0344kg/s$ .

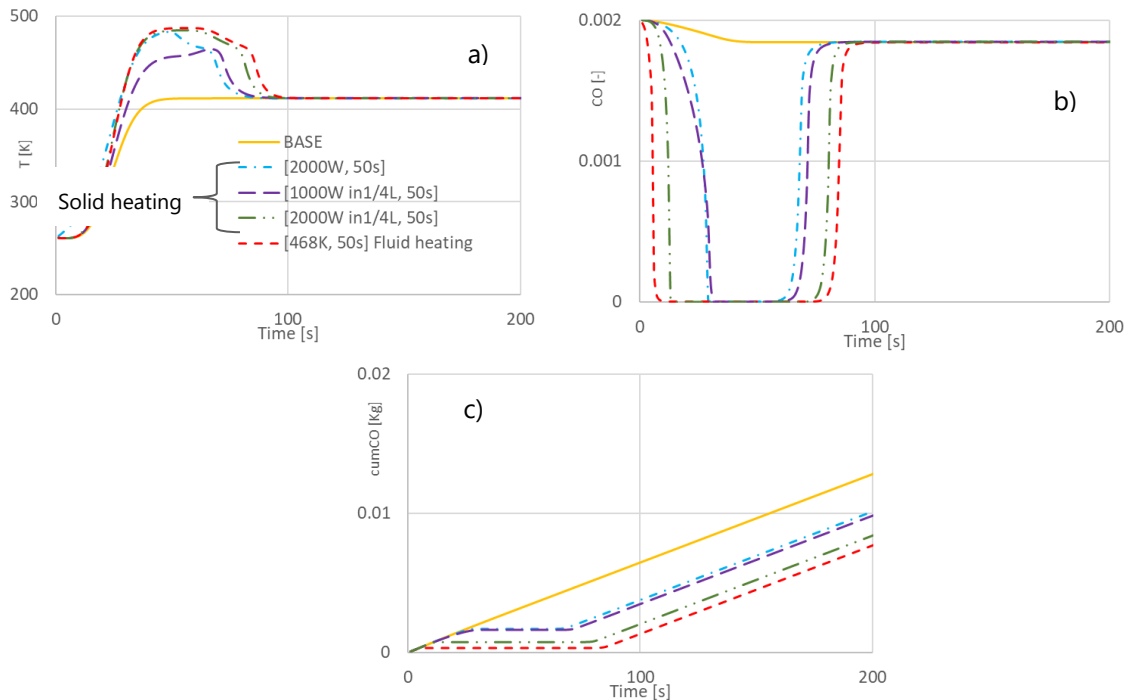


Fig. 20. Fluid temperature (a), CO mass concentration (b) and CO cumulative emissions (c) in time at  $x=L$  with  $T_{Fin}=410K$ ,  $T_s(t=0)=260K$ ,  $\dot{m}_F=0.0344kg/s$ .

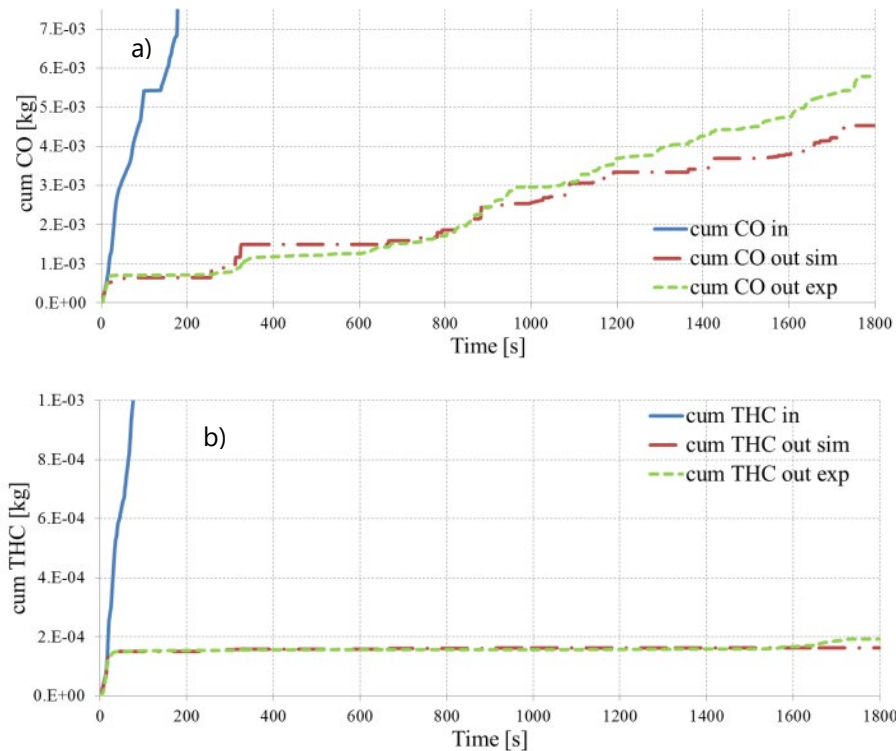
Fig. 20 shows the temperature, CO concentration and CO cumulative emissions time history at the converter exit for the different heating strategies considered already in Fig. 19 for the case of  $T_{Fin}=410K$  and  $T_s(t=0)=260K$  and  $\dot{m}_F=0.0344kg/s$ . Considering the same parameters in the case of lower  $\dot{m}_F$ , it is noticed that:

- The transient condition lasts less and steady state is reached earlier in time in the case with higher  $\dot{m}_F$ .
- Full conversion is reached with all the heating strategies with different durations, but at steady state only a small portion of CO is converted, leading to a linear increase of cumulative CO emissions (Fig. 20c).

- At higher  $\dot{m}_F$ , the strategy of heating the first converter quarter results in similar effects than heating the fluid. It can be deduced that, for low  $\dot{m}_F$ , it is more efficient to heat the fluid, while for increasing  $\dot{m}_F$ , the strategy of efficiently heating the converter becomes more promising.

### 3.8 Simulations of entire WLTC cycle: comparison between experiments and simulations

The results of the simulation model in Axisuite are compared with vehicle measurements on the chassis dynamometer in Fig. 21. Cumulative emissions of CO, THC and NOx downstream the catalytic converter during the WLTC cycle are plotted in function of time. In Table 9 experimental and simulated cumulative emissions during the overall cycle, but also in the first 300s have been reported. Overall, emissions are very low, thus catalyst efficiency is very high. Moreover, the model predicts experiments with good accuracy: simulations are able to exactly reproduce NO and THC cumulative emissions, while CO emissions are slightly underestimated by simulations. Even the evolution in time is captured with sufficient accuracy. However, there are some limited variations that simulations show and which are not seen in experiments. These can be related to the nature of the experimental setup which consists in relatively long pipe connections from the measuring locations to the exhaust gas analyzers and the different responses of the different measurement devices. These inaccuracies are encountered only in temperatures well above light-off temperature; therefore they do not affect the accuracy of simulations of pollutant emissions [19]. In these simulations, measured THC has been modelled as consisting of only  $C_3H_6$ . Fig. 21 clearly shows that the cycle emissions comprise mainly cold start contribution and partly discrete emission break-through events during transients. This is evident especially in simulations, less in experiments where the results are smoothed by the measurement setup. In the next sections the chemical mechanisms pertinent for each event type related to THC and NO are analyzed in detail. Considerations about CO reactions mechanisms are not reported because already discussed in detail in OpenFOAM results in the previous chapters.



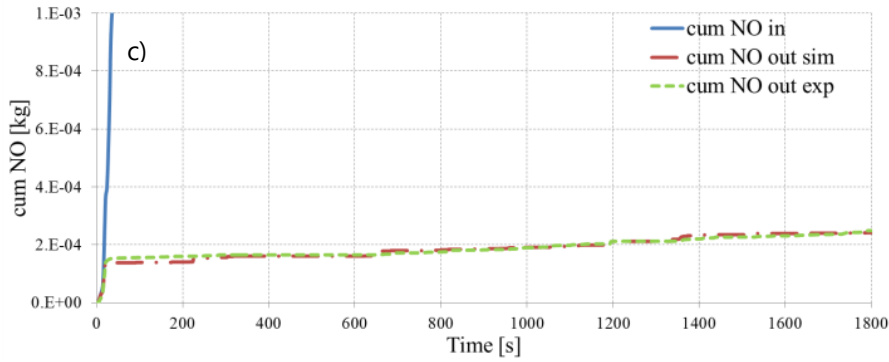


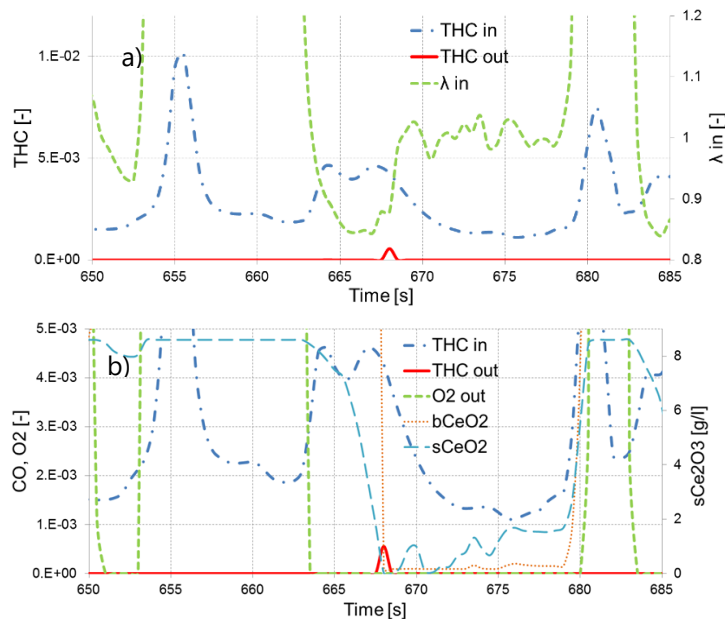
Fig .21. Comparison of measured and simulated cumulative exhaust emissions of CO (a), THC (b), and NO (c) in time.

Table 9. Cumulative exhaust emissions of CO, THC and NO in [kg], experimental and simulated in the first 300s and in the overall WLTC cycle.

	Experiments	Simulations	Experiments cold start	Simulations cold start
CO	0.00579	0.00453	0.00079	0.000918
THC	0.000192	0.000162	0.000154	0.000156
NO	0.000249	0.000241	0.000165	0.000157

### 3.8.1 THC emission peaks during warm phase

Fig. 22 analyzes one THC peak occurring around 670s. All THC peaks in the warm cycle phase have very similar structure of the underlying reaction mechanisms. Moreover, THC peaks are similar and synchronous with CO peaks. Figs. 22a-b describe the  $THC_{in}$  and  $THC_{out}$  trend, as well as the fuel air equivalence ratio,  $\lambda$  (a), and  $O_2$ ,  $bCeO_2$   $sCeO_2$  (b), while Fig. 22c reports all THC relevant reaction rates. THC peaks occur after a reacceleration period characterized by a rich mixture ( $\lambda > 1$ ) coming from the engine, with lack of  $O_2$ .  $CeO_2$  (both surface and bulk) react with  $C_3H_6$  till they are depleted. Immediately after, the THC peak occurs. THC peak diminishes thanks to reactions with surface ceria. On the whole, the main reactions occurring are direct oxidation, the ones with surface and bulk ceria, but also those with water (steam).



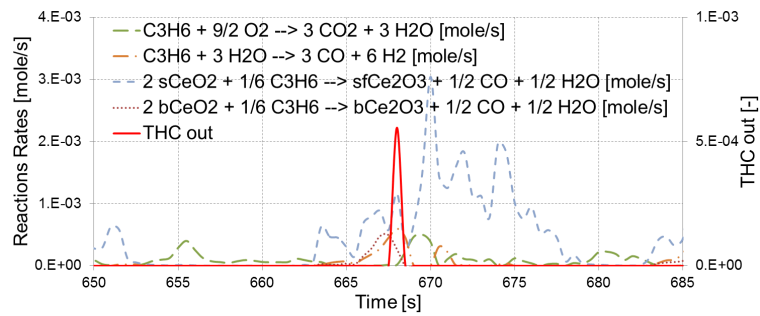


Fig. 22. Chemical reaction mechanisms related to a discrete THC emission peak around 668s.

### 3.8.2 NO emission peaks during warm phase

NO emissions mechanism differs from the one of THC: Fig. 23 describes the characteristics of NO peak during the warm phase of the cycle. NO peaks are not synchronized with CO and THC emissions. NO concentrations entering ( $NO_{in}$ ) and exiting ( $NO_{out}$ ) the catalytic converter are plotted in addition to the vehicle velocity profile in Fig. 23a and in addition to  $\lambda_{in}$  in Figs. 23b-c describes the rates of the most important reactions involved. The main mechanisms for the NO depletion are reduction with CO and surface ceria reactions, but also with  $H_2$ . NO peak occurs after a lean phase ( $\lambda_{in} > 1$ ): the engine-out NO ( $NO_{in}$  for the catalytic converter) is high but there is not enough CO and  $H_2$  from the engine, and  $sCe_2O_3$  for reactions to happen. Because the temperature is high enough, the reactions are limited by the mass transfer phenomena at the washcoat surface.

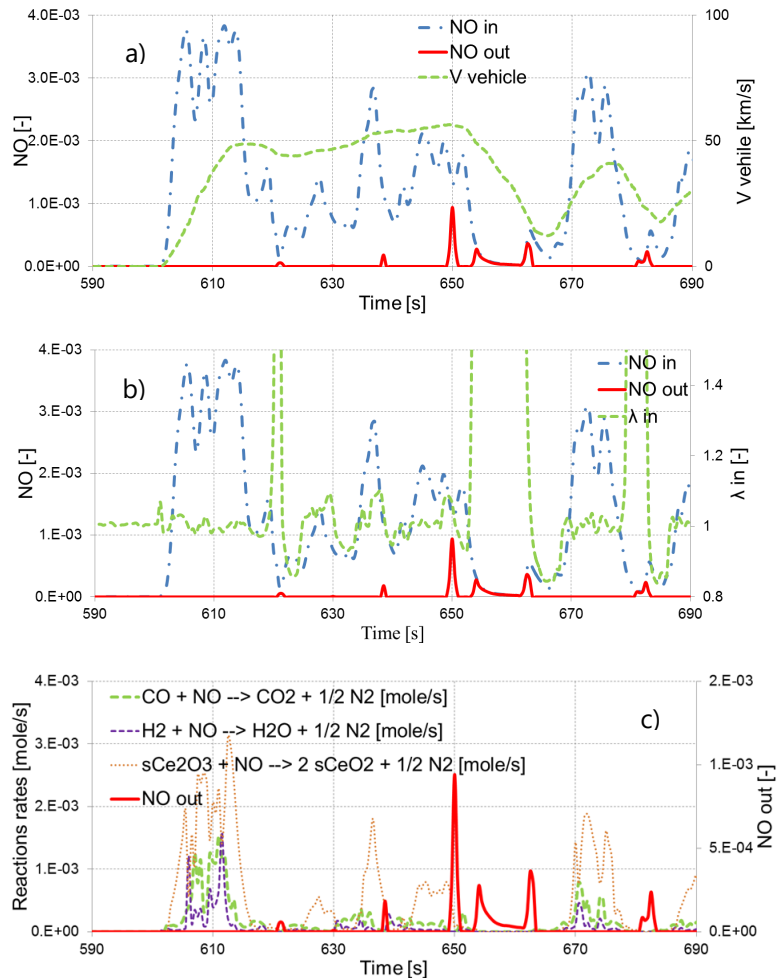


Fig. 23. Chemical reaction mechanisms related to a discrete NO emission peak around 610s.

### 3.8.3 Cold start emissions

According to simulation results, 20.3% of CO, 96.4% of THC and 64.8% of NO emissions happen in the first 300s of the WLTC cycle (300s taken as time limit for cold start period). Figs. 24 a-b report cumulative emission time histories for THC and NO and gas temperatures at the catalytic converter inlet respectively. During cold starts no reactions are evident in the catalytic converter before the temperature of the entering gas reaches 270°C (this occurs around time=20s).

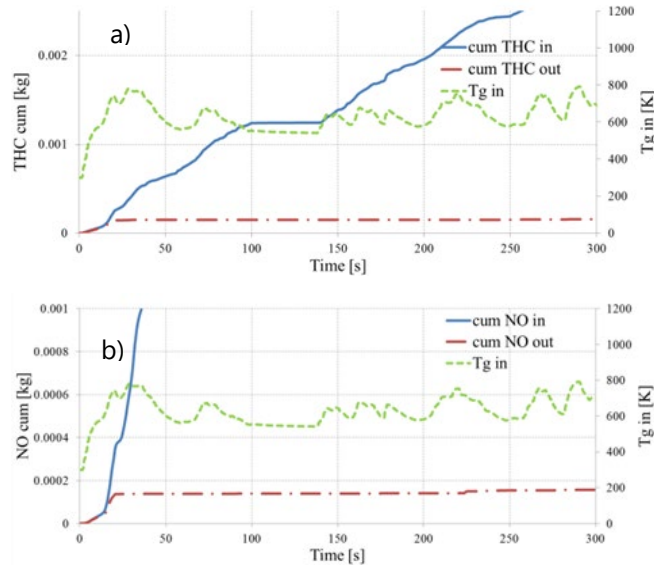
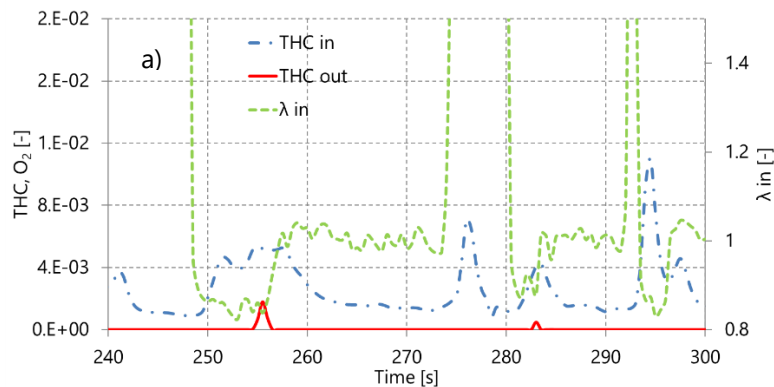


Fig. 24. Cold start cumulative and instantaneous emissions in the first 300s of a WLTC cycle. The exhaust gas temperature at the converter inlet is also plotted in the graph.

### 3.8.4 THC cold start emissions

Fig. 25 studies THC peaks during cold starts at 255s and 282s. In Fig. 25a instantaneous  $\text{THC}_{\text{in}}$  and  $\text{THC}_{\text{out}}$  are reported with  $\lambda_{\text{in}}$ , while Fig. 25b shows the reaction rates history. It is evident that the most important reaction mechanisms for THC depletion are surface ceria reactions and direct oxidation. The mechanism describing THC in the warm phase also characterizes the cold start period: emissions peaks happen after a deceleration, at the beginning of a phase of engine fuel cutoff, where the mixture is rich.  $\text{THC}_{\text{in}}$  coming from the engine is high, the  $\text{O}_2$  is depleted and there is low  $\text{sCe}_2\text{O}_3$  left, thus no direct oxidations and surface ceria reaction can occur.



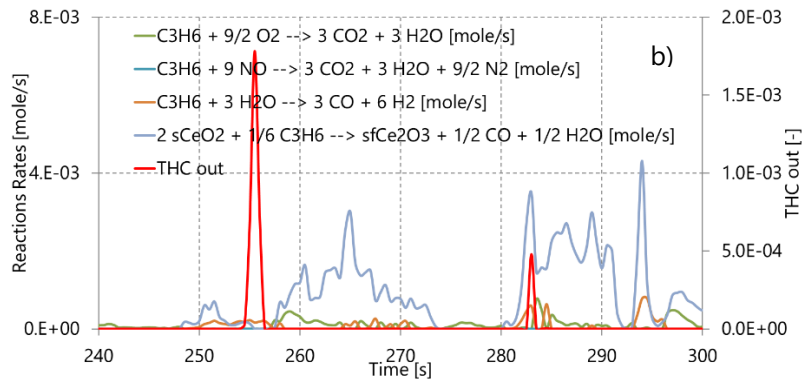


Fig. 25. Chemical reaction mechanisms related to THC oxidation during cold start.

### 3.8.5 NO cold start emissions

Fig. 26 describes NO reaction mechanisms during cold starts in the time interval [200,300]s. Plotted are instantaneous concentrations upstream ( $\text{NO}_{\text{in}}$ ), and downstream ( $\text{NO}_{\text{out}}$ ) the catalytic converter with the fuel air equivalence ratio,  $\lambda_{\text{in}}$  (Fig. 26a). Moreover, all relevant reaction rates (Fig. 26b) are reported. First of all, only some very small NO emissions occur. NO emissions happen during deceleration and thus lean periods. The main mechanisms for NO depletion remain the reactions with CO, H<sub>2</sub> and with surface ceria, as it happens during warm phases. Emissions happen when sCe<sub>2</sub>O<sub>3</sub>, CO and H<sub>2</sub> are not enough for the total reduction of NO.

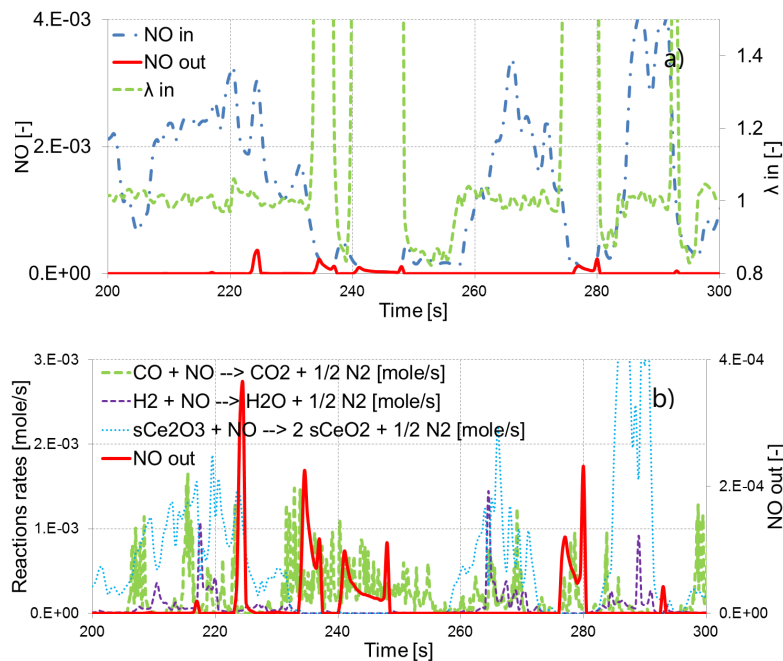


Fig. 26. Cold starts chemical reaction mechanisms related to NO emissions in the time range [200,300]s.

### 3.8.6 Analysis of the sensitivity of result emissions to $\lambda$ variation

The analysis conducted in the previous paragraphs has shown the importance of O<sub>2</sub> concentrations for the reactions in the catalytic converter. Fig. 27 investigates the effects of richer and leaner (both 5%) mixture entering the catalytic converter. Cumulative emissions results are reported for THC (Fig. 27a) and NO (Fig. 27b) respectively. The cumulative conversions, both over the entire WLTC cycle and only in

the first 300s, have been also reported in Table 10. On the whole, higher O<sub>2</sub> content increases CO and THC oxidation, but decreases dramatically NO reduction. On the contrary, lower O<sub>2</sub> has exactly the opposite effects.

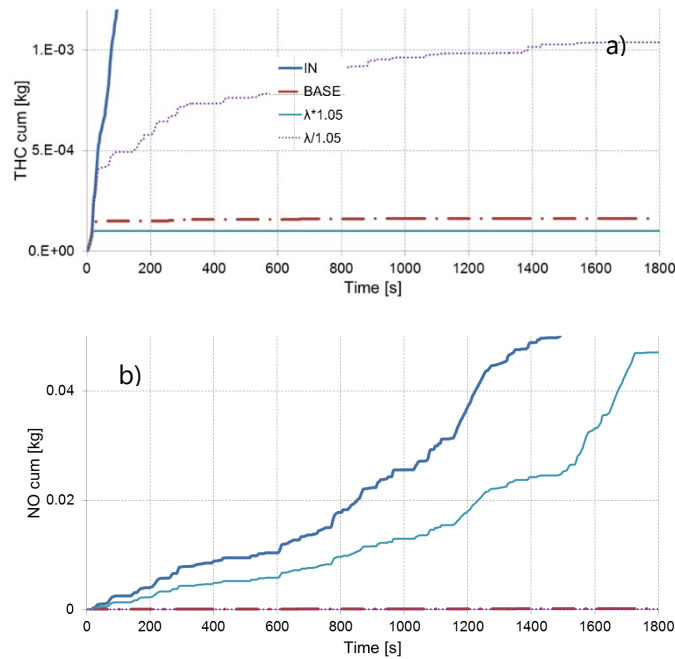


Fig. 27. Cumulative emissions for different average  $\lambda$ , THC (a), NO (b).

Table 10. Cumulative efficiency of CO, THC and NO with different  $\lambda$  both on the overall WLTC cycle and on the first 300s (cc=cold starts).

	$\eta_{CO}$ [%]	$\eta_{THC}$ [%]	$\eta_{NO}$ [%]	$\eta_{CO_{cc}}$ [%]	$\eta_{THC_{cc}}$ [%]	$\eta_{NO_{cc}}$ [%]
BASE	96.9	99.3	99.7	94.6	95.1	98.0
$\lambda*1.05$	99.7	99.5	51.1	97.7	96.8	44.2
$\lambda/1.05$	33.0	95.2	99.8	35.7	77.4	98.7

### 3.8.7 Effects of different PGM loadings of the catalyst

Simulations have been performed with the same amount of washcoat, decreased to 50% and to 20%. Results are reported in terms of cumulative emissions of THC and NO in Fig. 28 and corresponding cumulative efficiencies have been reported in Table 11, both considering the entire WLTC cycle and only the first 300s. The catalytic converter behaviour remains almost the same and emissions are still combination of cold start emissions and discrete break-through events. The time properties remain the same, but, according to predictions, emissions slightly increase with decreasing PGM. With 50% less PGM, conversion efficiency decreases of 0.3% for THC, while with only 20% of PGM, conversion decreases 0.5% for THC. NO reduction remains very high and does not vary significantly. Moreover, the impact of PGM is stronger on cold starts emissions.

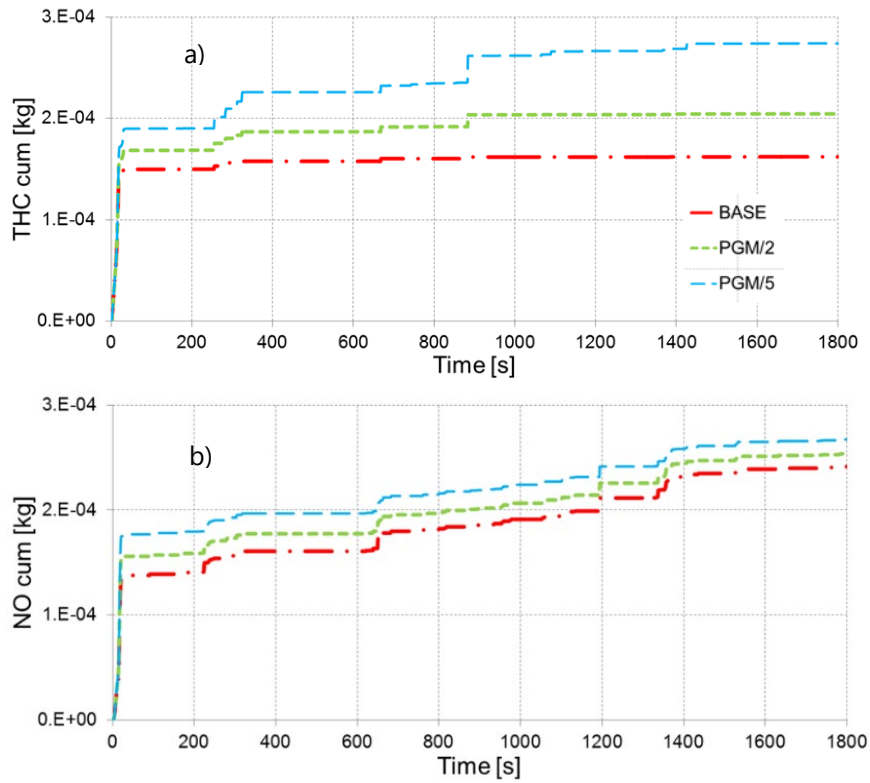


Fig. 28. Cumulative emissions with different P(latin) G(roup) M(etals) amounts in the catalyst coating, THC (a), NO (b).

Table 11. Cumulative efficiency of CO, THC and NO with different PGM loadings of the catalyst on the overall WLTC cycle and on the first 300s.

	$\eta_{CO}$ [%]	$\eta_{THC}$ [%]	$\eta_{NO}$ [%]	$\eta_{COcc}$ [%]	$\eta_{THCcc}$ [%]	$\eta_{NOcc}$ [%]
BASE	96.9	99.3	99.8	94.6	95.1	98.0
PGM/2	96.6	99.1	99.7	93.9	94.3	97.8
PGM/5	96.3	98.7	99.7	93.1	93.4	97.6

### 3.9 Simulations of other driving cycles

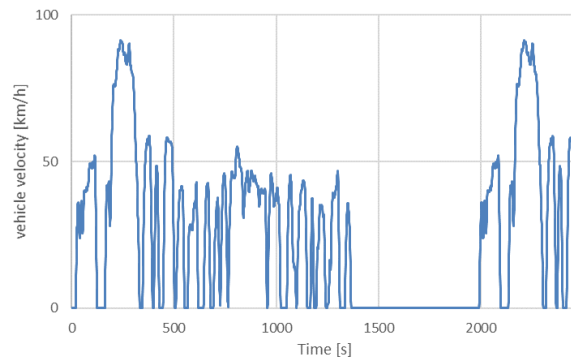


Fig. 29. FTP-75 cycle: vehicle velocity profile.

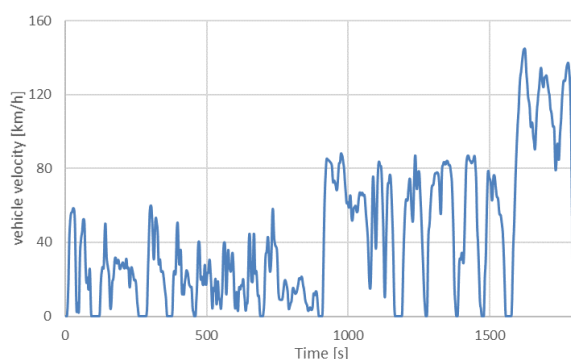


Fig. 30. RDEmax cycle: vehicle velocity profile.

In addition to the WLTC, further driving cycles have been tested on the chassis dynamometer with the same vehicle and same converter. Fig. 29 shows the EPA Federal Test Procedure, commonly known as FTP-75 for the city driving cycle, in terms of vehicle velocity in time, while Fig. 30 shows another driving cycle, the RDEmax. These two cycles have been simulated in Axisuite with the same reaction library described in Section 3.3, tuned with WLTC experimental results.

The results of the simulation model are compared with vehicle measurements in the case of the FTP-75 test procedure in Fig. 31. Cumulative emissions of CO, THC and NO<sub>x</sub> downstream the catalytic converter during the cycle are plotted in function of time. In addition, the cumulative O<sub>2</sub> exiting the converter is reported. In Table 12 simulated and experimental cumulative efficiencies of the overall cycle have been reported.

Table 12. Cumulative efficiencies of CO, THC and NO, measured and simulated over the FTP-75 cycle.

	Simulations	Experiments
CO	90.8%	71.8%
THC	94.1%	88.6%
NO	97.3%	96.6%

Overall, emissions are very low, thus catalyst efficiency is very high. The evolution in time is captured with sufficient accuracy and the fuel cutoff phases are well predicted. However, the model underestimates experimental emissions and overestimates the gas temperature. In particular, for all the three species, a big difference is during cold starts: In simulations, reactions initiate earlier with respect to experiments.

NO<sub>x</sub> emissions show the best prediction, with a discrepancy of 1% in cumulative efficiency. The difference is attributed to an overestimation of the reaction rates related to NO<sub>x</sub> reduction through CO and surface ceria. Simulations are able to replicate experimental peak emissions detected at  $t \approx 164s$  (during cold starts) and at  $t = 1994s$ , but with a visible time delay. THC conversions are mainly due to reactions with surface ceria and O<sub>2</sub>, but also due to steam reforming. Simulations are able to replicate the THC cumulative emissions trend: after cold starts, there is a period of moderate emissions, then a stage of full conversion and after  $t \approx 1995s$  new emissions. Due to the higher predicted temperature, however, THC emissions are everywhere underestimated (of  $\approx 6\%$  in cumulative efficiencies). This discrepancy is also due to the fact that in the model, THC have been modelled as consisting of only C<sub>3</sub>H<sub>6</sub>. Higher accuracy can be achieved if also C<sub>3</sub>H<sub>8</sub> and CH<sub>4</sub> are added. CO cumulative emissions are not well predicted and the

rates of its oxidation and its reaction with surface ceria are overestimated. This is confirmed by the O<sub>2</sub> cumulative emissions at the converter outlet: in simulations, more O<sub>2</sub> is consumed.

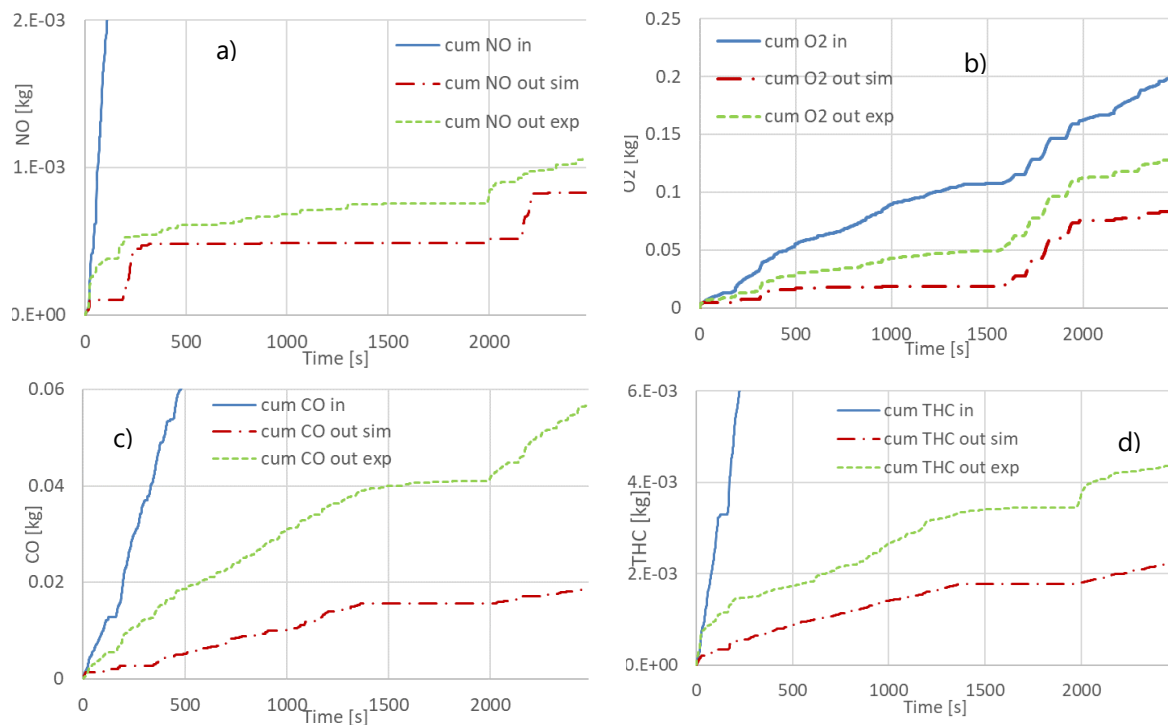


Fig. 31. Comparison of simulated and measured cumulative exhaust emissions of CO (a), THC (b), NO (c) and O<sub>2</sub> (d) in time over FTP-75 cycle.

The simulations are compared with vehicle measurements in the case of the RDEmax cycle in Fig. 32. Cumulative emissions of CO, THC and NO<sub>x</sub> downstream the catalytic converter during the cycle are plotted in function of time. In addition, the cumulative O<sub>2</sub> exiting the converter is reported. In Table 13 simulated and experimental cumulative efficiencies of the overall cycle have been reported.

Considerations already made for the FTP-75 cycle are still valid for the EPA test cycle: even in this case, the model underestimates experimental emissions of CO, C<sub>3</sub>H<sub>6</sub> and O<sub>2</sub> and overestimates the gas temperature and the NO<sub>x</sub> consumption. Even the main reaction mechanisms already described for Fig. 31 are here valid. However, in this case, NO emissions are well predicted during cold starts, but overestimated at the end of the cycle.

Interestingly, the trends are well captured, however the values have significant differences. It seems that the model is developed based only on the measurements of the WLTC cycle is appropriate. The parametrization should happen with the goal to minimize the deviation of the simulations to the experiments in all three cycles. So a combined approach will lead to higher accuracy.

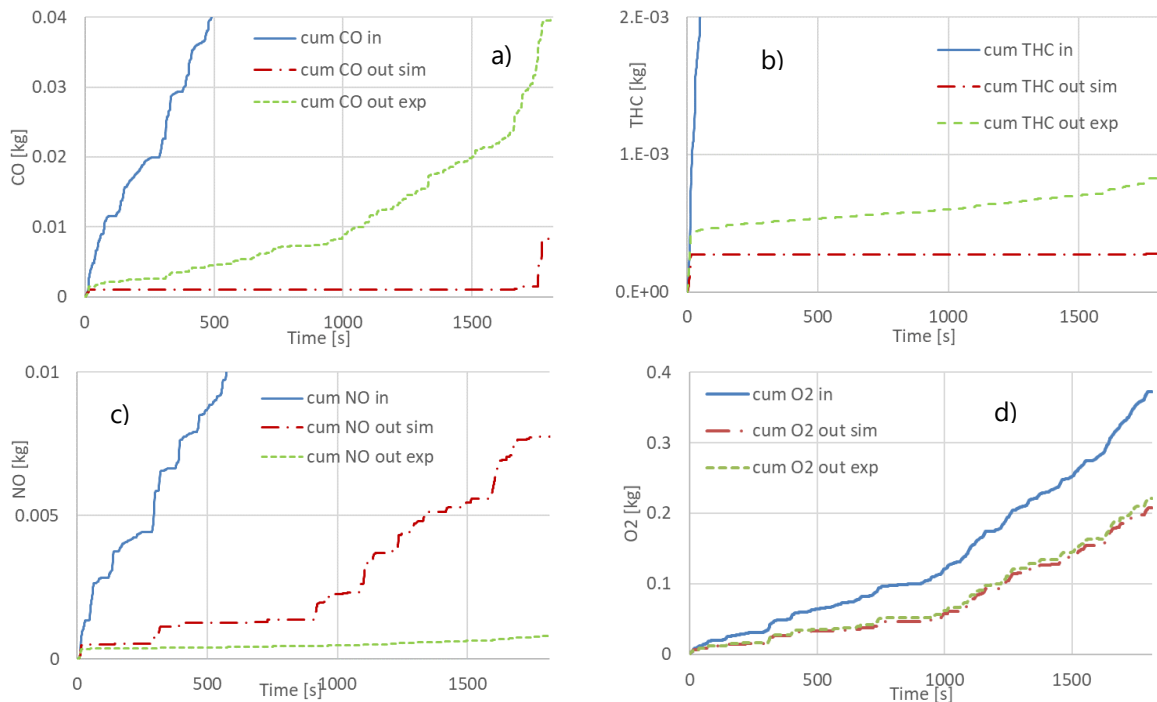


Fig .32. Comparison of simulated and measured cumulative exhaust emissions of CO (a), THC (b), NO (c) and O<sub>2</sub> (d) in time over RDEmax cycle.

Table 13. Cumulative efficiencies of CO, THC and NO in [-], experimental and simulated over a FTP-75 cycle.

	Simulations	Experiments
CO	96.9%	85.5%
THC	89.0%	98.9%
NO	99.5%	98.5%

## References

- [1] OpenFOAM, "OpenFOAM documentation," <http://www.openfoam.org/docs/>
- [2] F. Lucci, A. Della Torre, G. Montenegro, R. Kaufmann, P. Dimopoulos Eggenschwiler, Comparison of geometrical, momentum and mass transfer characteristics of real foams to Kelvin cell lattices for catalyst applications, *Int.J. Heat Mass Transf.* 108, 341–350, , 2017.
- [3] V. Papetti, P. Dimopoulos Eggenschwiler, A. Della Torre, F. Lucci, A. Ortona, G. Montenegro, Additive Manufactured open cell polyhedral structures as substrates for automotive catalysts, *Int.J. Heat Mass Transf.* 126, 1035-1047, <https://doi.org/10.1016/j.ijheatmasstransfer.2018.06.61>, 2018
- [4] A. Della Torre, G. Montenegro, A. Onorati, T. Cerri, CFD Investigation of the Impact of Electrical Heating on the Light-off of a Diesel Oxidation Catalyst, SAE International, 2018.
- [5] F. Lucci, A. Della Torre, G. Montenegro, P. Dimopoulos Eggenschwiler, On the catalytic performance of open cell structures versus honeycombs, *Chem. Eng. J.* 264 514–521, 2015. <https://doi.org/10.1016/j.cej.2014.11.080>.
- [6] S.E. Voltz, C.R. Morgan, D. Liederman, S.M. Jacob, *Ind. Eng. Chem. Prod. Res. Dev.* 12 294, 1973.
- [7] G.C. Koltsakis, , A.M. Stamatelos, P.A. Konstantinidis, Development and Application Range of Mathematical Models for 3-Way Catalytic Converters, *Applied Catalysis B: Environmental*, 1997.
- [8] G. Koltsakis, Warm-Up Behavior of Monolithic Reactors Under Non-Reacting Conditions, *Chem. Eng. Sci.* 53:2891- 2899, 1997.

- [9] S.H. Oh, J.C. Cavendish and L.L. Hegedus, *AIChE J.*, 26 (1980) 935.
- [10] W. M. Yan, Y. L. Tsay, T. F. Lin, Transient conjugated heat transfer in laminar pipe flows, *Int. J. Heat Mass Transfer* 32(4), 775-777, 1989
- [11] E. Bianchi, T. Heidig, C.G. Visconti, G. Groppi, H. Freund, E. Tronconi, An appraisal of the heat transfer properties of metallic open-cell foams for strongly exo-/endo-thermic catalytic processes in tubular reactors, *Chem. Eng. J.* 198–199(August), 512–528, 2012.
- [12] R. E. Hayes, S. T. Kolaczkowski, Mass and heat transfer effects in catalytic monolith reactors, *Chem. Engn. Sci.* 49(21), 3587-3599, 1994.
- [13] W. M. Kays, M. E. Crawford, *Convective Heat and Mass Transfer*, 3rd Ed. McGraw-Hill, New York, U.S.A, 1993.
- [14] Brettschneider J.: Berechnung des Luftverhältnisses  $\lambda$  von Luft-Kraftstoff-Gemischen und des Einflusses von Messfehlern auf  $\lambda$ , *Bosch Technische Berichte* 6 (1979).
- [15] Brettschneider J.: Extension of the equation for calculation of the air-fuel equivalence ratio, *SAE International*, 972989, (1997).
- [16] V. Papetti, P. Dimopoulos Eggenschwiler, A. Della Torre, G. Montenegro, A. Onorati, G. Koltsakis, Heat Transfer Analysis of Catalytic Converters during Cold Starts, *SAE (Society of Automotive Engineers) Paper*, 2019-24-0163, <https://doi.org/10.4271/2019-24-0163>, 2019
- [17] V. Papetti, P. Dimopoulos Eggenschwiler, A. della Torre, G. Montenegro, A. Onorati, A. Ortona, G. Koltsakis, Stationary Heat and Mass Transfer phenomena in Additive Manufactured Open Cell Polyhedral Structures for Automotive Catalysis, *Open Cell Polyhedral Structures.*, *Chemical Engineering Science* or its open access mirror, Ref: CES-D-20-01857, under review.
- [18] V. Papetti, P. Dimopoulos Eggenschwiler, Reduction of Cold Start emissions with Microwave heated Catalytic converters, *Proceedings of the 19th Stuttgart International Symposium, Automotive and Engine Technology*, [https://doi.org/10.1007/978-3-658-25939-6\\_51](https://doi.org/10.1007/978-3-658-25939-6_51), 2019.
- [19] J. Sucec, An improved quasi-steady approach for transient conjugated forced convection problems, *Int. J. Heat Mass Transfer*. 24, 1711-1722.